

Impact of grids and dynamical cores in CESM2.2 on the surface mass balance of the Greenland Ice Sheet

Adam R. Herrington¹, Peter H. Lauritzen¹, Marcus Lofverstrom², William H. Lipscomb¹, Andrew Gettelman¹ and Mark A. Taylor³

¹National Center for Atmospheric Research, 1850 Table Mesa Drive, Boulder, Colorado, USA

²Department of Geosciences, University of Arizona, 1040 E. 4th Street, Tucson, Arizona USA

³Sandia National Laboratories, Albuquerque, New Mexico, USA

Key Points:

- The CESM2.2 release includes several enhancements to the spectral-element dynamical core, including two Arctic refined mesh configurations.
- Uniform resolution grids degrade the Greenland Ice Sheet mass balance compared to equivalent resolution latitude-longitude grids.
- The refined Arctic meshes substantially improve the surface mass balance over all low resolution grids.

15 **Abstract**

16 Six different configurations, a mixture of grids and atmospheric dynamical cores
 17 available in the Community Earth System Model, version 2.2 (CESM2.2), are evaluated
 18 for their skill in representing the climate of the Arctic and the surface mass balance of
 19 the Greenland Ice Sheet (GrIS). The conventional 1° – 2° uniform resolution grids sys-
 20 tematically overestimate both accumulation and ablation over the GrIS. Of these con-
 21 ventional grids, the latitude-longitude grids outperform the quasi-uniform unstructured
 22 grids because they have more degrees of freedom to represent the GrIS. Two Arctic-refined
 23 meshes, with $1/4^{\circ}$ and $1/8^{\circ}$ refinement over Greenland, are documented as newly sup-
 24 ported configurations in CESM2.2. The Arctic meshes substantially improve the sim-
 25 ultated clouds and precipitation rates in the Arctic. Over Greenland, these meshes skill-
 26 fully represent accumulation and ablation processes, leading to a more realistic GrIS sur-
 27 face mass balance. As CESM is in the process of transitioning away from conventional
 28 latitude-longitude grids, these new Arctic-refined meshes improve the representation of
 29 polar processes in CESM by recovering resolution lost in the transition to quasi-uniform
 30 grids.

31 **Plain Language Summary**

32 The mass balance of Earth's big ice sheets is crucially important for understand-
 33 ing controls on global sea-level rise. However, the scale of the processes needed to rep-
 34 resent ice sheet mass balance is challenging to resolve in conventional Earth System Mod-
 35 els. This study evaluates the ability of different grids and atmospheric solvers (i.e., the
 36 dynamical core) in CESM2.2 to resolve the surface mass balance (SMB) of the Green-
 37 land Ice Sheet. We show that the ongoing transition away from latitude longitude grids,
 38 towards quasi-uniform unstructured grids in CESM2.2 leads to a degradation of the sim-
 39 ultated SMB. Two variable-resolution grids with enhanced resolution over Greenland are
 40 developed and incorporated into the release of CESM2.2, which substantially improves
 41 the SMB over the latitude longitude grids.

42 **1 Introduction**

43 General Circulation Models (GCMs) are powerful tools for understanding the me-
 44 teorology and climate of the high latitudes, which are among the most sensitive regions
 45 on Earth to global and environmental change. GCMs differ vastly in their numerical treat-
 46 ment of polar regions because of the so-called *pole problem* (Williamson, 2007). The pole
 47 problem refers to numerical instability arising from the convergence of meridian lines into
 48 polar singularities on latitude-longitude grids (e.g., Figure 1a, hereafter referred to as
 49 *lat-lon* grids). Depending on the numerics, methods exist to suppress this instability, and
 50 lat-lon grids may be advantageous for polar processes by representing structures with
 51 finer resolution than elsewhere in the computational domain. With the recent trend to-
 52 wards globally uniform unstructured grids, any potential benefits of lat-lon grids in po-
 53 lar regions may be lost. In this study, we evaluate a number of grids and dynamical cores
 54 (hereafter referred to as *dycores*) available in the Community Earth System Model, ver-
 55 sion 2.2 (CESM2.2; Danabasoglu et al., 2020), including new variable-resolution grids,
 56 to understand their impacts on the simulated Arctic climate. We focus specifically on
 57 the climate and surface mass balance of the Greenland Ice Sheet.

58 In the 1970s, the pole problem was largely defeated through the adoption of effi-
 59 cient spectral transform methods in GCMs (see Williamson, 2007, and references therein).
 60 These methods transform grid point fields into a global, isotropic representation in wave
 61 space, where linear operators (e.g., horizontal derivatives) in the (truncated) equation
 62 set can be solved exactly. While spectral transform methods are still used today, local
 63 numerical methods have become desirable for their ability to run efficiently on massively

parallel systems. The pole problem has thus re-emerged in contemporary climate models that use lat-lon grids, and some combination of reduced grids (modified lat-lon grids, with cells elongated in the longitudinal direction over the polar regions) and polar filters are necessary to ameliorate this numerical instability (Jablonowski & Williamson, 2011). Polar filters subdue the growth of unstable computational modes by applying additional damping to the numerical solution over polar regions. This damping reduces the effective resolution in polar regions such that the resolved scales are *approximately* the same everywhere on the grid. We emphasize *approximately*, since it is conceivable that marginal increases in effective resolution occur over polar regions in lat-lon grids, despite polar filtering, since resolved waves can be represented with more grid points than at lower latitudes.

Dycores built on lat-lon grids have some advantages over unstructured grids. Lat-lon coordinate lines are orthogonal, and aligned with zonally symmetric circulations that characterize many large-scale features of Earth's atmosphere. Lauritzen et al. (2010) has experimented with rotating lat-lon models such that their coordinate lines no longer align with an idealized, zonally balanced circulation. For the finite-volume lat-lon dycore considered in this paper (hereafter *FV*), numerical errors were shown to be largest when the polar singularity is rotated into the baroclinic zone (45°N latitude), generating spurious wave growth much earlier in the simulation than for other rotation angles. This illustrates the advantages of coordinate surfaces aligned with latitude bands, albeit an extreme example where the polar singularity and the polar filter are also contributing to the spurious wave growth. The unstructured grids all generate spurious baroclinic waves earlier in the simulations than the (unrotated) lat-lon models, although the unstructured model considered in this paper, the spectral-element dycore (hereafter *SE*), holds a balanced zonal flow without spurious wave growth appreciably longer than the rotated FV experiments (Lauritzen et al., 2010). And unlike FV, the SE dycore has the same error characteristics regardless of how the grid is rotated.

The polar filter in the FV model impedes efficiency at large processor (CPU) counts because it requires a spectral transform, which have large communication overhead (Suarez & Takacs, 1995; Dennis et al., 2012). Unstructured grids support quasi-uniform grid spacing globally, and there is no pole problem (e.g., Figure 1c). Conversely, unstructured grids are becoming more common due to their improved performance on massively parallel systems and lack of constraints on grid structure (Taylor et al., 1997; Putman & Lin, 2007; Wan et al., 2013). This grid flexibility allows for the adoption of variable-resolution grids (e.g., Figure 2; hereafter abbreviated as *VR*), sometimes referred to as regional grid refinement. In principle, grid refinement over polar regions can make up for any loss of resolution in transitioning away from lat-lon grids (e.g., Figure 2). However, local grid refinement comes at the cost of a smaller CFL-limited time step in the refined region; the CFL-condition — short for Courant–Friedrichs–Lewy condition — is a necessary condition for numerical stability when using discrete data in time and space.

We emphasize that the pole problem is a distinctive feature of the dycore in atmospheric models. Polar filters do not directly interfere with the physical parameterizations, nor do they have any bearing on the surface models; e.g., the land model can take full advantage of the greater number of grid cells in polar regions on lat-lon grids. This is particularly relevant for the surface mass balance of the Greenland Ice Sheet (*SMB*; the integrated sum of precipitation and runoff), which relies on hydrological processes represented in the land model.

The SMB of the Greenland Ice Sheet (hereafter *GrIS*) is determined by processes occurring over a range of scales that are difficult to represent in GCMs (Pollard, 2010). GrIS precipitation is concentrated at the ice-sheet margins, where steep topographic slopes drive orographic precipitation. The truncated topography used by low resolution GCMs enables moisture to penetrate well into the GrIS interior, manifesting as a positive precipitation bias (Pollard & Groups, 2000; van Kampenhout et al., 2018). GrIS ablation

117 areas (marginal regions where seasonal melting exceeds the annual mass input from pre-
 118 precipitation) are typically less than 100 km wide and are confined to low-lying areas or re-
 119 gions with low precipitation. These narrow ablation zones are not fully resolved in low-
 120 resolution GCMs, and may further degrade the simulated SMB. For example, CESM,
 121 version 2.0 (CESM2) underestimates ablation in the northern GrIS, leading to unreal-
 122 istic ice advance when run with an interactive ice sheet component (Lofverstrom et al.,
 123 2020).

124 Regional climate models (RCMs) are commonly relied upon to provide more ac-
 125 curate SMB estimates. The limited area domain used by RCMs permits the use of high-
 126 resolution grids capable of resolving SMB processes, and can skillfully simulate the GrIS
 127 SMB (Box et al., 2004; Rae et al., 2012; Van Angelen et al., 2012; Fettweis et al., 2013;
 128 Mottram et al., 2017; Noël et al., 2018). However, unlike GCMs, RCMs are not a freely
 129 evolving system, and the atmospheric state must be prescribed at the lateral boundaries
 130 of the model domain. The inability of the RCM solution to influence larger-scale dynam-
 131 ics outside the RCM domain (due to the prescribed boundary conditions) severely lim-
 132 its this approach from properly representing the role of the GrIS in the climate system.
 133 In addition, the boundary conditions are derived from a separate host model, which in-
 134 troduces inconsistencies due to differences in model design between the host model and
 135 the RCM.

136 In order to retain the benefits of RCMs in a GCM, van Kampenhout et al. (2018)
 137 used the VR capabilities of the SE dycore in CESM, generating a grid where Greenland
 138 is represented with $1/4^\circ$ resolution, and elsewhere with the more conventional 1° reso-
 139 lution. The simulated SMB compared favorably to the SMB from RCMs and observa-
 140 tions. The VR approach is therefore emerging as a powerful tool for simulating and un-
 141 derstanding the GrIS and its response to different forcing scenarios.

142 The SE dycore has been included in the model since CESM version 1, but has been
 143 under active development ever since. This includes the switch to a dry-mass vertical co-
 144 ordinate (Lauritzen et al., 2018) and incorporation of an accelerated multi-tracer trans-
 145 port scheme (Lauritzen et al., 2017), made available in CESM2. This paper documents
 146 several additional enhancements to the SE dycore as part of the release of CESM2.2. These
 147 include three new VR configurations (Figure 2), two Arctic meshes and a Contiguous
 148 United-States mesh (CONUS; featured in Pfister et al. (2020)). While there are dozens of
 149 published studies using VR in CESM (e.g., Zarzycki et al., 2014; Rhoades et al., 2016;
 150 Gettelman et al., 2017; Burakowski et al., 2019; Bambach et al., 2021), these studies ei-
 151 ther used development code or collaborated closely with model developers. CESM2.2 is
 152 the first code release that contains out-of-the-box VR functionality.

153 This study compares the representation of Arctic regions using the SE and FV
 154 dycores in CESM2.2 (see description below), as these two dycores treat high latitudes (i.e.,
 155 the pole problem) in different ways. Section 2 documents the grids, dycores, and phys-
 156 ical parameterizations used in this study, and also describes the experiments, datasets,
 157 and evaluation methods. Section 3 analyzes the results of the experiments, and Section 4
 158 provides a general discussion and conclusions.

159 2 Methods

160 2.1 Dynamical cores

161 The atmospheric component of CESM2.2 (Danabasoglu et al., 2020), the Commu-
 162 nity Atmosphere Model, version 6.3 (CAM6; Gettelman et al., 2019; Craig et al., 2021),
 163 supports several different atmospheric dynamical cores. These include dycores on lat-
 164 ion grids, such as finite-volume (FV; Lin, 2004) and Eulerian spectral transform (EUL;
 165 Collins et al., 2006) models, and dycores built on unstructured grids, including spectral-
 166 element (SE; Lauritzen et al., 2018) and finite-volume 3 (FV3; Putman & Lin, 2007) mod-

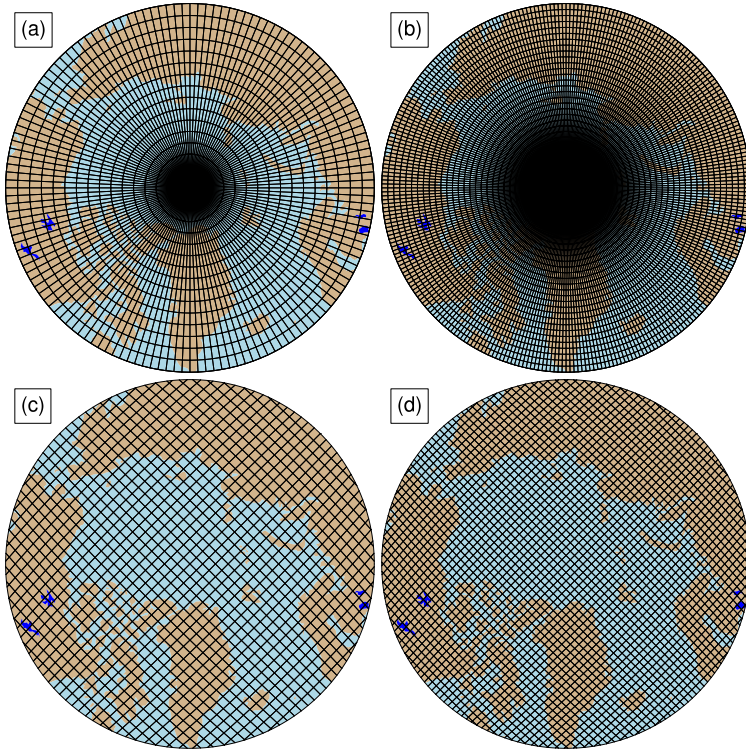


Figure 1. Computational grids for the uniform $1^\circ - 2^\circ$ grids in this study. Grids names after Table 1, (a) f19, (b) f09, (c) ne30pg2 and (d) ne30pg3.

els. This study compares the performance of the SE and FV dycores, omitting the EUL and FV3 dycores. CESM2 runs submitted to the Coupled Model Intercomparison Project Phase 6 (Eyring et al., 2016) used the FV dycore, whereas the SE dycore is often used for global high-resolution simulations (e.g., Small et al., 2014; Bacmeister & Coauthors, 2018; Chang et al., 2020) due to its higher throughput on massively parallel systems (Dennis et al., 2012).

2.1.1 Finite-volume (FV) dynamical core

The FV dycore is a hydrostatic model that integrates the equations of motion using a finite-volume discretization on a spherical lat-lon grid (Lin & Rood, 1997). The 2D dynamics evolve in floating Lagrangian layers that are periodically mapped to an Eulerian reference grid in the vertical (Lin, 2004). Hyperviscous damping is applied to the divergent modes, and is increased in the top few layers (referred to as a *sponge layer*) to prevent undesirable interactions with the model top, such as wave reflection (Lauritzen et al., 2011). A polar filter damps computational instability due to the convergence of meridians, permitting a longer time step. It takes the form of a Fourier filter in the zonal direction, with the damping coefficients increasing monotonically in the meridional direction (Suarez & Takacs, 1995). The form of the filter is designed to slow down the propagation of large zonal wave-numbers to satisfy the CFL condition of the shortest resolved wave at some reference latitude.

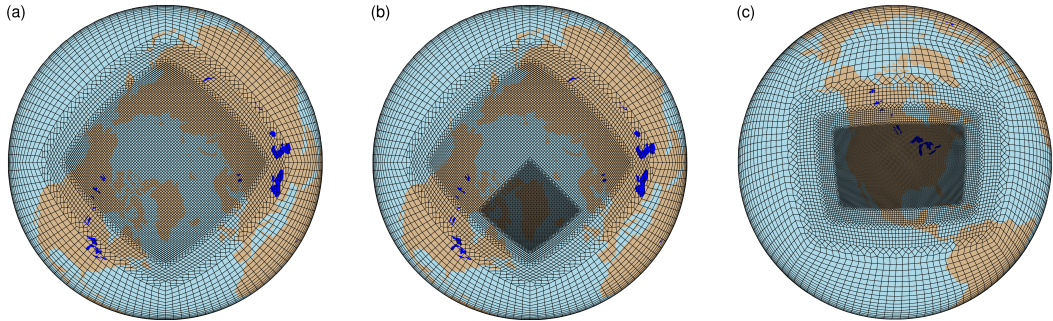


Figure 2. Variable-resolution grids available in CESM2.2, (a) **Arctic**, (b) **Arctic - GrIS** and (c) **CONUS**. Note what is shown is the element grid; the computational grid has 3×3 independent grid points per element.

186 2.1.2 Spectral-element (SE) dynamical core

187 The SE dycore is a hydrostatic model that integrates the equations of motion us-
 188 ing a high-order continuous Galerkin method (Taylor et al., 1997; Taylor & Fournier, 2010).
 189 The computational domain is a cubed-sphere grid tiled with quadrilateral elements (see
 190 Figure 2). Each element contains a fourth-order basis set in each horizontal direction,
 191 with the solution defined at the roots of the basis functions, the Gauss-Lobatto-Legendre
 192 quadrature points. This results in 16 nodal points per element, with 12 of the points ly-
 193 ing on the (shared) element boundary. Communication between elements uses the di-
 194 rect stiffness summation (Canuto et al., 2007), which applies a numerical flux to the el-
 195 ement boundaries to reconcile overlapping nodal values and produce a continuous global
 196 basis set.

197 As with the FV dycore, the dynamics evolve in floating Lagrangian layers that are
 198 subsequently mapped to an Eulerian reference grid. A dry mass vertical coordinate was
 199 recently implemented for thermodynamic consistency with condensates (Lauritzen et al.,
 200 2018). The 2D dynamics have no implicit dissipation, and so hyperviscosity operators
 201 are applied to all prognostic variables to remove spurious numerical errors (Dennis et
 202 al., 2012). Laplacian damping is applied in the sponge layer.

203 In CESM2.2, the SE numerics have been enhanced to mitigate spurious noise over
 204 topography. These algorithmic changes are described in Appendix A.

205 The SE dycore supports regional grid refinement via its VR configuration, requir-
 206 ing two enhancements over uniform-resolution setups. First, as the numerical viscosity
 207 increases with resolution, explicit hyperviscosity relaxes according to the local element
 208 size, reducing in strength by an order of magnitude per halving of the grid spacing. A
 209 tensor-hyperviscosity formulation is used (Guba et al., 2014), which adjusts the coeffi-
 210 cients in two orthogonal directions to more accurately target highly distorted quadrilat-
 211 eral elements. Second, the topography boundary conditions are smoothed in a way that
 212 does not excite grid scale modes, and so the NCAR topography software (Lauritzen et
 213 al., 2015) has been modified to scale the smoothing radius by the local element size, re-
 214 sulting in rougher topography in the refinement zone.

215 For SE grids with quasi-uniform grid spacing, the SE tracer transport scheme is
 216 replaced with the Conservative Semi-Lagrangian Multi-tracer transport scheme (CSLAM)
 217 (Lauritzen et al., 2017). Atmospheric tracers have large, nearly discontinuous horizon-
 218 tal gradients that are difficult to represent with spectral methods, which are prone to
 219 oscillatory “Gibbs-ringing” errors (Rasch & Williamson, 1990). CSLAM has improved

grid name	dycore	Δx_{eq} (km)	Δx_{refine} (km)	Δt_{phys} (s)
f19	FV	278	-	1800
f09	FV	139	-	1800
ne30pg2	SE-CSLAM	167	-	1800
ne30pg3	SE-CSLAM	111	-	1800
ne30pg3*	SE-CSLAM	111	-	450
Arctic	SE	111	28	450
Arctic – GrIS	SE	111	14	225

Table 1. Grids and dycores used in this study. Δx_{eq} is the average equatorial grid spacing, Δx_{refine} is the grid spacing in the refined region (if applicable), and Δt_{phys} is the physics time step. FV refers to the finite-volume dycore, SE the spectral-element dycore, and SE-CSLAM the spectral-element dycore with CSLAM tracer advection. We use the ne30pg3 grid for two runs with different values of Δt_{phys} .

tracer property preservation and accelerated multi-tracer transport. It uses a separate grid from the spectral-element dynamics, dividing each element into 3×3 control volumes with quasi-equal area. The physical parameterizations are computed from the state on the CSLAM grid, which has clear advantages over the original SE dycore in which the physics are evaluated Gauss-Lobatto-Legendre points (Herrington et al., 2018).

2.2 Grids

We evaluate model simulations on six different grids in this study (Table 1). The FV dycore is run with nominal 1° and 2° grid spacing, referred to as f09 and f19, respectively (Figure 1a,b). We also run the 1° equivalent of the SE-CSLAM grid, referred to as ne30pg3 (Figure 1d), where ne refers to a grid with $ne \times ne$ quadrilateral elements per cubed-sphere face, and pg denotes that there are $pg \times pg$ control volumes per element for computing the physics. We run an additional 1° SE-CSLAM simulation with the physical parameterizations computed on a grid with 2×2 control volumes per element, ne30pg2 (Figure 1c; Herrington et al., 2019, note CSLAM is still run on the 3×3 control volume grid).

Three VR meshes were developed for the CESM2.2 release to support grid refinement over the Arctic and the United States (Figure 2). This paper serves as the official documentation of these grids. The VR meshes were developed using the software package SQuadgen (<https://github.com/ClimateGlobalChange/squadgen>). The Arctic grid is a 1° grid with $1/4^\circ$ regional refinement over the broader Arctic region. The Arctic–GrIS grid is identical to the Arctic grid, but with an additional patch covering the island of Greenland with $1/8^\circ$ resolution. The CONUS grid contains $1/8^\circ$ refinement over the United States, and 1° everywhere else. The CONUS grid is not discussed any further in this paper; see Pfister et al. (2020) for simulations with the CONUS grid.

The accuracy of the simulated surface mass balance is expected to be sensitive to grid resolution. Figure 3a shows the average grid spacing over the Greenland Ice Sheet (*GrIS* hereafter) in all six grids in this study. The ne30pg2 grid has the coarsest representation with an average grid spacing (Δx) of $\Delta x = 160$ km, and the Arctic–GrIS grid has the highest resolution with an average grid spacing of $\Delta x = 14.6$ km, similar to the 11 km grid spacing of the RACMO2.3 grid. The ne30pg3 grid has an average $\Delta x = 111.2$ km, substantially coarser than the f09 grid, with an average $\Delta x = 60$ km. Although ne30pg3 and f09 have similar average grid spacing over the entire globe, and comparable computational costs, the convergence of meridians on the FV grid enhances the resolution over the GrIS. The Arctic grid has an average grid spacing of $\Delta x = 27.8$ km, and is about 10 times more expensive than the 1° models. The Arctic–GrIS grid is about twice as expensive as the Arctic grid.

The physics time step depends on the grid resolution. Increased horizontal resolution permits faster vertical velocities that reduce characteristic time scales, so the physics time step is reduced to avoid large time truncation errors (Herrington & Reed, 2018). The `Arctic` and `Arctic - GrIS` grids are run with a $4\times$ and $8\times$ reduction in physics time step relative to the default 1800 s time step used in the 1° and 2° grids (Table 1).

All grids and dycores in this study use 32 hybrid pressure-sigma levels in the vertical, with a model top of 2 hPa or about 40 km. However, any grid or dycore can in principle be run with a higher model top or finer vertical resolution.

2.3 Physical parameterizations

All simulations in this study use the CAM6 physical parameterization package (hereafter referred to as the *physics*; Gettelman et al., 2019). The physics in CAM6 differs from its predecessors through the incorporation of high-order turbulence closure, Cloud Layers Unified by Binormals (CLUBB; Golaz et al., 2002; Bogenschutz et al., 2013), which jointly acts as a planetary boundary layer, shallow convection, and cloud macrophysics scheme. CLUBB is coupled with the MG2 microphysics scheme (Gettelman & Morrison, 2015; Gettelman et al., 2015), which computes prognostic precipitation and uses classical nucleation theory to represent cloud ice for improved cloud-aerosol interactions. Deep convection is parameterized using a convective quasi-equilibrium mass flux scheme (Zhang & McFarlane, 1995; Neale et al., 2008) and includes convective momentum transport (Richter et al., 2010). Boundary layer form drag is modeled after Beljaars et al. (2004), and orographic gravity wave drag is represented with an anisotropic method informed by the orientation of topographic ridges at the sub-grid scale (the ridge orientation is derived from a high-resolution, global topography dataset (J. J. Danielson & Gesch, 2011)).

Initial simulations with the `ne30pg3` SE grid produced weaker shortwave cloud forcing relative to the tuned finite-volume dycore in the standard CESM2 configuration. The SE dycore in CESM2.2 therefore has two CLUBB parameter changes to provide more realistic cloud forcing and top-of-atmosphere radiation balance. We reduced the width of the sub-grid distribution of vertical velocity (`clubb_gamma` = 0.308 → 0.270) and also reduced the strength of the damping for horizontal component of turbulent energy (`clubb_c14` = 2.2 → 1.6) to increase cloudiness. For a description of how CLUBB parameters impact the simulated climate, see Guo et al. (2015).

2.4 Simulated surface mass balance (SMB)

All grids and dycores simulate the GrIS SMB, which is the sum of mass accumulation from precipitation and mass loss from ablation. The latter is the sum of evaporation, sublimation and liquid runoff, with runoff being a combination of liquid precipitation and snow and ice melt. Not all liquid precipitation or snow/ice melt runs off the ice sheet; this water can penetrate pore spaces in the snowpack/firn layer and freeze, forming ice lenses. These relevant SMB processes are represented by different CESM components, but it is the Community Land Model, version 5 (CLM; Lawrence et al., 2019), that aggregates these processes and computes the SMB.

CLM runs on the same grid as the atmosphere, and uses a downscaling technique to account for sub-grid variability in SMB. In short, the ice sheet patch in a CLM grid cell is subdivided into 10 elevation classes (ECs), each with a distinct surface energy balance and SMB. The area fraction of each EC is derived from a high-resolution GrIS elevation dataset. The near-surface air temperature, humidity, and air density are calculated for each EC using an assumed lapse rate and the elevation difference from the grid-cell mean. Precipitation from CAM is repartitioned into solid or liquid based on the surface temperature of the EC; precipitation falls as snow for temperatures between $T < -2^\circ\text{ C}$, as rain for $T > 0^\circ\text{ C}$, and as a linear combination of rain and snow for temper-

data product	years used in this study	resolution	citation
ERA5	1979-1998	1/4°	Copernicus (2019)
CERES-EBAF ED4.1	2003-2020	1°	Loeb et al. (2018)
CALIPSO-GOCCP	2006-2017	1°	Chepfer et al. (2010)
RACMO2.3	1979-1998	11 km	Noël et al. (2015)
RACMO2.3p2	1979-1998	5.5 km	Noël et al. (2019)

Table 2. Description of observational datasets used in this study.

305 atures between -2° C and 0° C. Snow accumulation in each EC is limited to a depth
 306 of 10 m liquid water equivalent. Any snow above the 10 m cap contributes towards ice
 307 accumulation in the SMB, and refreezing of liquid water within the snowpack is an ad-
 308 ditional source of ice. Integrating over all ECs, weighting by the area fractions, provides
 309 a more accurate SMB than would be found using the grid-cell mean elevation. For a more
 310 detailed description of how the SMB is computed in CESM, we refer the reader to Lipscomb
 311 et al. (2013); Sellevold et al. (2019); van Kampenhout et al. (2020); Muntjewerf et al.
 312 (2021).

313 Changes in ice depth, but not snow depth, count toward the SMB. That is, snow
 314 accumulation above the 10 m cap contributes a positive SMB, and surface ice melting
 315 (after melting of the overlying snow) yields a negative SMB. Since snow in the accumu-
 316 lation zone must reach the cap to simulate a positive SMB, the snow depths on the VR
 317 grids were spun up by forcing CLM in standalone mode, cycling over data from a 20-
 318 year Arctic FHISt simulation (a model simulation with prescribed, observed sea-surface
 319 conditions) for about 500 years. The uniform-resolution grids are initialized with the SMB
 320 from an existing f09 spun-up initial condition. In the simulations described here, the
 321 GrIS is prescribed at its observed, modern extent and thickness.

322 2.5 Observational Datasets

323 We use several observational datasets (Table 2) to assess the performance of the
 324 simulations. SMB datasets are gathered from multiple sources. Regional Atmospheric
 325 Climate Model, version 2.3 11km (RACMO2.3; Noël et al., 2015) and version 2.3p2 5.5km
 326 (RACMO2.3p2; Noël et al., 2018, 2019) are RCM simulations targeting Greenland, forced
 327 by ERA reanalyses products at the domain's lateral boundaries. The RACMO simula-
 328 tions have been shown to perform skillfully against observations and are often used as
 329 modeling targets (e.g., Evans et al., 2019; van Kampenhout et al., 2020).

330 In-situ SMB (snow pit and ice cores) and radar accumulation datasets (e.g., Ice-
 331 Bridge) are maintained in The Land Ice Verification and Validation toolkit (LIVVkit),
 332 version 2.1 (Evans et al., 2019). However, these point-wise measurements are difficult
 333 to compare to model output spanning several different grids, especially since the SMB
 334 from each elevation class is not available from the model output. We used a nearest-neighbor
 335 technique for an initial analysis, which showed that the model biases are similar to those
 336 computed using the RACMO datasets. Because of the uncertainty of comparing grid-
 337 ded fields to point-wise measurements, and the lack of information added with regard
 338 to model biases, we omitted these datasets from our analysis.

339 2.6 SMB Analysis

340 We seek to integrate SMB components over a GrIS ice mask and to diagnose their
 341 contributions to the GrIS mass budget. However, the ice masks vary across the grids,
 342 especially in comparison to the RACMO3.2 ice mask, whose total area is about 3% less
 343 than that of the reference dataset (Figure 3b). CLM's dataset creation tool generates
 344 the model ice mask by mapping a high-resolution dataset to the target grid using the

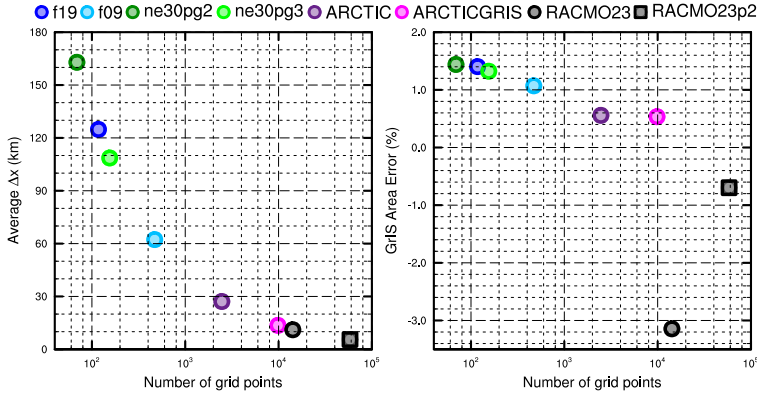


Figure 3. The spatial properties of the GrIS as represented by different grids in this study. (Left) GrIS area error, computed as the relative differences from a 4-km dataset used to create the CESM ice masks, (right) approximate average grid spacing over GrIS.

345 Earth System Modeling Framework (ESMF) first-order conservative remapping algorithm
 346 (Team et al., 2021). The figure suggests that the mapping errors are less than 1.5% across
 347 the CESM2 grids. The area errors in Figure 3b may seem small, but even 1–2% area
 348 differences can lead to large differences in integrated SMB (Hansen et al., 2022).

349 We have taken a common-ice-mask approach by mapping all model fields to the
 350 lowest-resolution grids, i.e., the f19 and ne30pg2 grids, and integrating over these low-
 351 resolution ice masks. The use of low-resolution common ice masks is a conservative de-
 352 cision, and is justified because we seek to use first-order remapping algorithms to map
 353 fields to the common ice mask, which is not generally reliable when mapping to a higher-
 354 resolution grid than the source grid. We use two remapping algorithms: ESMF first-order
 355 conservative and the TempestRemap (Ullrich & Taylor, 2015) high-order monotone al-
 356 gorithm. Since mapping errors are sensitive to grid type, we evaluate all quantities on
 357 both common ice masks, the f19 and ne30pg2 masks. Thus, we evaluate an integrated
 358 quantity on a given grid up to four times to estimate the uncertainty due to differences
 359 in grid type and remapping algorithms.

360 The SMB is expressed in a form that is agnostic of water phase, a total water mass
 361 balance, to facilitate comparisons across different grids with different ice masks and to
 362 increase consistency with the variables available in the RACMO datasets. The SMB for
 363 total water can be expressed as:

$$SMB = accumulation + runoff + evaporation/sublimation, \quad (1)$$

364 where all terms have consistent sign conventions (positive values contribute mass, and
 365 negative values reduce mass). The accumulation source term refers to the combined solid
 366 and liquid precipitation, runoff refers to the liquid water sink, and evaporation/sublimation
 367 is the vapor sink. Since the runoff term aggregates many processes, we isolate the melt-
 368 ing contribution by also tracking the combined melt of snow and ice. Note that this SMB
 369 expression is different from the internally computed SMB described in section 2.4.

370 We consider two approaches for mapping and integrating the SMB components over
 371 the common ice masks:

- 372 1. Map the grid-cell mean quantities to the common grid, and integrate the mapped
 373 fields over the common ice masks.

- 374 2. Map the patch-level quantities (i.e., the state over the ice fractional component
 375 of the grid cell) to the common grid, and integrate the mapped fields over the com-
 376 mon ice masks.

377 Note that we are mapping to low-resolution grids that have larger GrIS areas than
 378 the source grids (Figure 3b). Since the components of equation 1 are not confined to the
 379 ice mask, method 1 reconstructs the SMB over the portion of the common ice mask that
 380 is outside the ice mask on the source grid. While this may be a an acceptable way to re-
 381 construct the mass source terms over different ice masks, ice melt is zero outside the source
 382 ice mask, and so method 1 will underestimate the mass sink term. This underestima-
 383 tion is systematic in method 2, where all variables are exclusive to the ice mask; map-
 384 ping to a lower-resolution grid will dilute a field of non-zero values over the ice mask with
 385 a field of zeros outside the ice mask. However, patch-level values for processes exclusive
 386 to the ice mask (e.g., ice melt) will on average have larger magnitudes than the grid-mean
 387 quantities used in method 1.

388 The different error characteristics of the two methods are used to diversify the en-
 389 semble. Each of the four regridding combinations (with conservative and high-order remap-
 390 ping to the f09 and ne30pg2 grids) are repeated with each method, resulting in (up to)
 391 eight values for each integrated quantity. Unfortunately, the patch-level values of evap-
 392 oration/sublimation are not available from the model output, and we estimate their con-
 393 tribution by zeroing out the field for grid cells that have no ice, prior to mapping to the
 394 common ice mask. This will degrade the SMB estimates using method 2, but we are more
 395 interested in characterizing the behavior of individual processes across grids and dycores,
 396 expressed as the components of the SMB, rather than the SMB itself.

397 2.7 Experimental design

398 All simulations described here use an identical transient 1979-1998 Atmospheric
 399 Model Inter-comparison Project (AMIP) configuration, with prescribed monthly sea-surface
 400 temperature and sea ice following Hurrell et al. (2008). In CESM terminology, AMIP
 401 simulations use the FHIST computational set and run out of the box in CESM2.2.

402 3 Results

403 3.1 Tropospheric temperatures

404 Before delving into the simulated Arctic climate conditions, we assess the global
 405 mean differences between the various grids and dycores. Figure 4 shows 1979-1998 an-
 406 nual mean, zonal mean height plots expressed as differences between uniform-resolution
 407 grids and dycores. The f09 grid is warmer than the f19 grid, primarily in the mid-to-
 408 high latitudes throughout the depth of the troposphere. This is a common response to
 409 increasing horizontal resolution in GCMs (Pope & Stratton, 2002; Roeckner et al., 2006).
 410 Herrington and Reed (2020) have shown that this occurs in CAM due to higher resolved
 411 vertical velocities which, in turn, generate more condensational heating in the CLUBB
 412 macrophyics. The right panel in Figure 4a supports this interpretation, showing an in-
 413 crease in the climatological CLUBB heating at all latitudes in the f09 grid, but with the
 414 largest increase in the mid-latitudes.

415 As the SE dycore is less diffusive than the FV dycore, the resolved vertical veloc-
 416 ities are larger in the SE dycore, and so the ne30pg3 troposphere is modestly warmer
 417 than f09 (Figure 4b). The stratosphere responds differently, with ne30pg3 much cooler
 418 than f09 in the mid-to-high latitudes. Figure 4c also shows small temperature differences
 419 between ne30pg3 and ne30pg2, with ne30pg3 slightly warmer near the tropopause at
 420 high latitudes. This is consistent with the similar climates found for these two grids by
 421 Herrington et al. (2019).

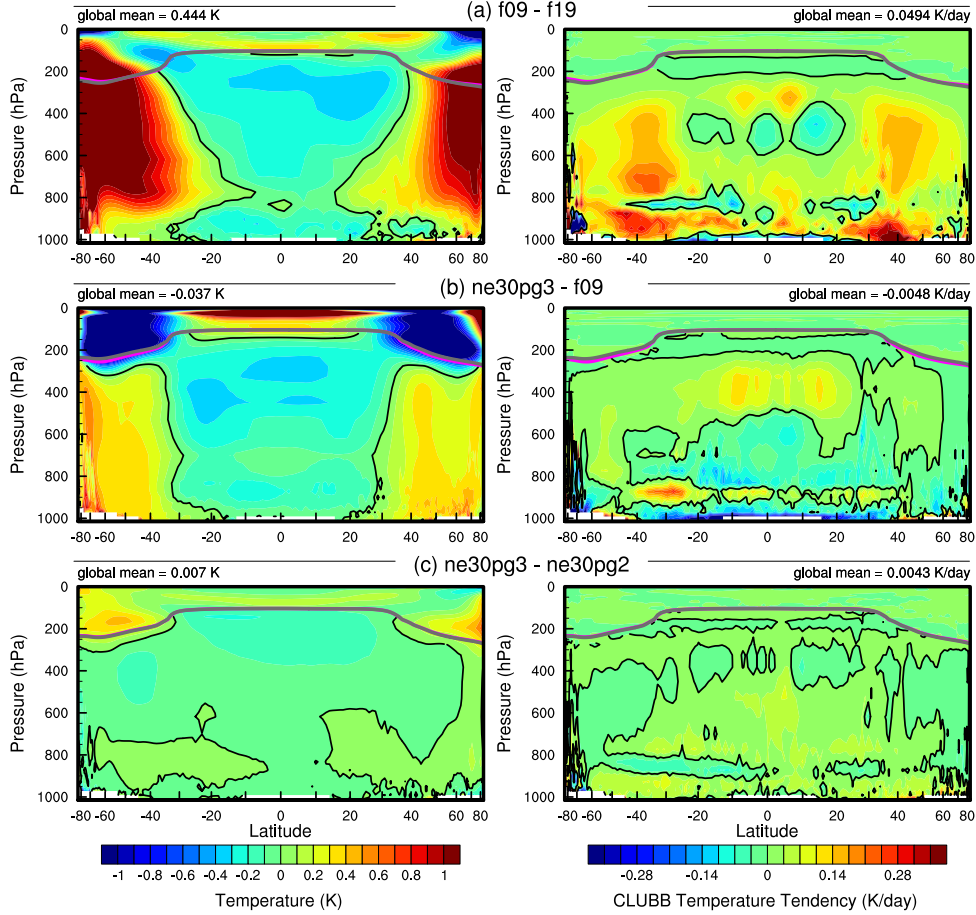


Figure 4. 1979–1998 annual mean temperature (left column) and CLUBB temperature tendencies (right column) in zonal mean height space, expressed as differences between the various $1^\circ - 2^\circ$ grids. The thick grey and magenta lines are the tropopause for the control run and the test run, respectively.

Comparing the VR grids to the uniform-resolution grids is complicated because we simultaneously increase the resolution and reduce the physics time-step, both of which influence the solution (Williamson, 2008). We therefore run an additional `ne30pg3` simulation with the shorter physics time step used in the `Arctic` grid (450 s), referred to as `ne30pg3*` (Table 1). Figure 5a shows the difference between `ne30pg3*` and `ne30pg3` for climatological summer temperatures in zonal-mean height space. The troposphere is warmer with the reduced time step, and the mechanism is similar in that the shorter time step increases resolved vertical velocities (not shown) and CLUBB heating (right panel in Figure 5a). Figure 5b shows the difference in climatological summer temperature between the `Arctic` grid and the `ne30pg3*` grid. With the same physics time step, the greater condensational heating and warmer temperatures are confined to the refined Arctic region.

Figure 5c shows that the `Arctic-GrIS` grid is much warmer than the `Arctic` grid in the Arctic summer. This may be due, in part, to the shorter physics time step, but the temperature response is too large to be explained by enhanced condensational heating from CLUBB alone. This summer warming appears to be a result of variations in the stationary wave pattern, with a swath of anomalous southerly winds to the west of

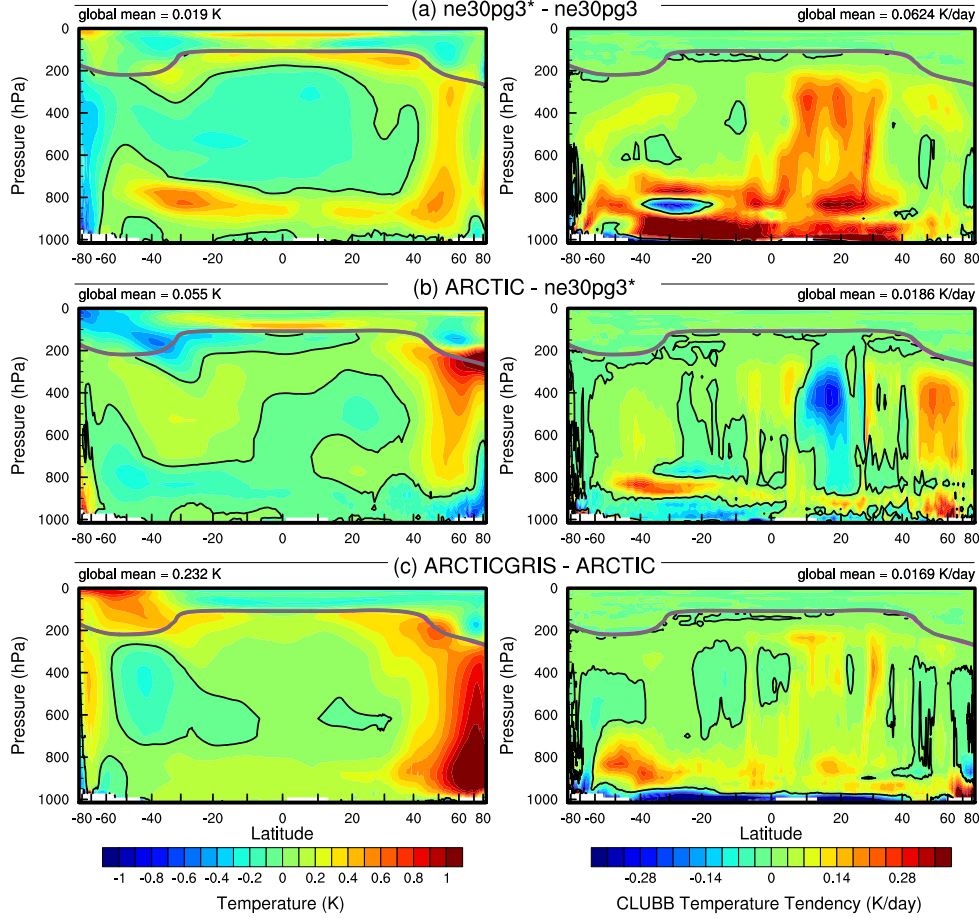


Figure 5. As in Figure 4 but for the short-time-step experiment and the VR grids. The fields plotted are for the climatological northern hemisphere summer. We focus on summer because that is when the resolution response is largest, and the refined regions are located in the northern hemisphere.

Greenland (not shown). This dynamic response is interesting, because other than the physics time step, the only difference between the Arctic – GrIS and Arctic runs is the doubling of resolution over Greenland. This behavior will be explored further in a future study.

It is useful to understand summer temperature biases due to their control on ice and snow melt over the GrIS (Ohmura, 2001). Figure 6 shows the 1979–1998 lower troposphere summer temperature bias relative to ERA5, computed by equating a layer mean virtual temperature with the 500–1000 hPa geopotential thickness. The results are consistent with the zonal mean height plots; increasing resolution from f19 to f09 warms the climate, and the 1° SE grids are warmer than the FV grids. The FV summer temperatures are persistently colder than ERA5, whereas the 1° SE grids are not as cold, and are actually warmer than ERA5 at high-latitudes, north of 75°. All grids show a north-south gradient in bias over Greenland, with the summer temperature bias more positive for the northern part of the ice sheet. This pattern is also evident in the near surface temperature bias over Greenland (not shown).

454 The **Arctic** grid has summer temperatures similar to the 1° SE grids, but is slightly
 455 warmer over northern Eurasia and the North Pole (Figure 6). An anomalous cooling patch
 456 forms to the west of Greenland, centered over Baffin Island. The **Arctic – GrIS** grid
 457 is warmer than the **Arctic** grid over most of the Arctic, but with a similar spatial pat-
 458 tern of summer temperature bias.

459 Some of these temperature differences may be related to differences in summer cloudi-
 460 ness. Figure 7 shows the summer shortwave cloud forcing bias in the six runs, using the
 461 CERES product. Shortwave cloud forcing quantifies the impact of clouds on shortwave
 462 radiation, taken as the difference between all-sky and clear-sky shortwave radiative fluxes
 463 at the top of the atmosphere. A negative bias corresponds to excessive reflection and cool-
 464 ing. The uniform grids have similar biases, with the clouds reflecting 20–40 W/m² too
 465 much shortwave radiation over a wide swath of the Arctic, primarily the land masses.
 466 There is also a halo of positive bias (clouds not reflective enough) around the ocean perime-
 467 ter of Greenland. The **Arctic** grid has much smaller cloud forcing biases over the Arc-
 468 tic land masses, but is still too reflective over Alaska, the Canadian Archipelago, and parts
 469 of Eurasia. Compared to the **Arctic** grid, the **Arctic – GrIS** grid vastly reduces the
 470 cloud forcing bias over Eurasia, and also improves the bias over North America. In both
 471 VR grids, the halo of positive shortwave cloud forcing bias around the perimeter of Green-
 472 land is absent.

473 The summer cloud forcing biases are consistent with the summer temperature bi-
 474 ases in Figure 6 – regions where clouds are too reflective coincide with regions that are
 475 too cold. While we have not quantified the contribution of cloud biases to the cooler Arc-
 476 tic temperatures, shortwave radiation is a crucial component of the Arctic energy bud-
 477 get during summer. The shortwave cloud forcing biases are on the order of 10 W/m²,
 478 which is a significant fraction of the total absorbed shortwave during Arctic summer (Serreze
 479 et al., 2007) and is therefore likely a factor contributing to the cooler temperatures.

480 3.2 Clouds and precipitation over Greenland

481 In addition to summer temperatures, shortwave radiation is an important deter-
 482 minant of snow and ice melt. Figure 8 shows the summer incident shortwave radiation
 483 bias at the surface over Greenland and surrounding seas. The top panel shows the bias
 484 relative to the RACMO2.3p2 dataset, and the middle panel relative to the CERES dataset.
 485 The halo of excessive incident shortwave radiation around the coasts of Greenland is ap-
 486 parent for both datasets in relation to the coarser grids, consistent with the shortwave
 487 cloud forcing biases in Figure 7.

488 The ice sheet interior receives too little shortwave radiation in the coarser grids.
 489 On the VR grids, both the interior shortwave deficit and the excessive shortwave around
 490 the ocean perimeter are improved. This suggests that the coarse grid clouds are too thick
 491 in the interior of Greenland and too thin around the perimeter, which is consistent with
 492 the total summer cloud fraction bias, computed from the CALIPSO cloud dataset and
 493 shown in the bottom panel of Figure 8. Note that total cloud fraction characterizes the
 494 cloud field at all vertical levels, and attenuates the changes arising from any single layer
 495 due to the occurrence of overlapping clouds at other levels. The VR grids exhibit an over-
 496 all improvement in total cloud fraction bias, relative to the coarse grids.

497 The top panel of Figure 9 shows the annual climatological mean precipitation bias
 498 over the GrIS, expressed as the fractional difference from the RACMO2.3p2 solution. The
 499 coarse $1^{\circ} – 2^{\circ}$ grids have large, positive biases centered over the southern dome. The
 500 **Arctic** grid reduces this bias substantially, and the **Arctic – GrIS** grid reduces it fur-
 501 ther, with precipitation centers migrating from the interior toward the margins.

502 The more accurate representation of orographic precipitation in the VR grids is con-
 503 sistent with the cloud and radiation biases, cf. Figures 7, 8, and 9. The agreement of the

grid name	accumulation	total melt	runoff	sublimation	SMB
RACMO	681.7 (733.5)	-318.6 (-436.4)	-189.1 (-258.5)	-34.5 (-38.8)	458.1 (436.2)
ne30pg2	1007. (973.4)	-519.9 (-647.3)	-381.9 (-347.0)	-33.9 (-32.1)	591.2 (594.3)
ne30pg3	931.0 (909.3)	-540.8 (-686.7)	-375.8 (-330.1)	-34.1 (-32.6)	521.2 (546.6)
f19	884.9 (913.5)	-414.0 (-546.5)	-284.0 (-284.3)	-36.5 (-37.5)	564.4 (591.7)
f09	873.9 (882.1)	-389.1 (-482.3)	-256.1 (-212.3)	-37.3 (-37.4)	580.5 (632.4)
Arctic	784.1 (818.6)	-335.5 (-436.8)	-215.8 (-194.2)	-42.4 (-43.9)	526.0 (580.5)
Arctic – GrIS	693.8 (747.3)	-437.3 (-610.4)	-276.8 (-307.8)	-48.1 (-51.8)	369.0 (387.7)

Table 3. 1979-1998 surface mass balance of the Greenland Ice Sheet in Gt/yr. Values shown are using the common ice mask approach described in the methods section, whereas values in parentheses are from integrating over the native grid and ice mask.

504 cloud, radiation and precipitation biases in and around Greenland from multiple independent datasets indicates that the biases are a robust feature of the coarser grids. The 505 reduced biases in the VR grids suggest that the deficiencies of the coarse grids are due 506 to insufficient horizontal resolution, consistent with previous findings that coarse GCMs 507 have large, positive precipitation biases over Greenland (Pollard & Groups, 2000; van 508 Kampenhout et al., 2018).

510 3.3 Greenland surface mass balance

511 Table 3 shows the 1979-1998 climatological SMB components for each grid, com- 512 pared with RACMO. The values in the table are averages over the ensemble of mapping 513 methods to the common ice masks described in section 2.6, and the RACMO values re- 514 fer to the average of both RACMO ensembles. Table 3 also contains (in parenthesis) the 515 SMB components derived from evaluating the integrals on each model’s native grid and 516 ice mask. Of note is the large reduction in melt rates compared to the values computed 517 on the native grid, illustrating the dissipation of this quantity discussed in section 2.6. 518 For integrated precipitation, the differences between the native and common ice mask 519 approaches are much smaller, since the combined solid/liquid precipitation rates are not 520 directly tied to the ice mask.

521 The coarse grids are characterized by too much precipitation and too much melt- 522 ing and runoff, compared with RACMO. The total SMB on coarse grids therefore has 523 smaller errors than the individual components (Table 3), because large errors in the source 524 and sink terms offset one another when added together. Such compensating errors un- 525 derlie the importance of understanding the extent to which a model is getting the right 526 SMB for the right reasons.

527 Figure 10 shows time series of annually integrated precipitation and snow/ice melt 528 over the GrIS for the various different grids and dycores, and RACMO in black. The 1979- 529 1998 climatological mean values from Table 3 are shown as circles on the right side of 530 the panels. The uniform $1^\circ - 2^\circ$ grids have positive precipitation biases, whereas the 531 VR grids have the smallest biases, with precipitation comparable to RACMO. The f19 532 and f09 grids perform similarly, with +110 Gt/yr bias, whereas ne30pg3 is biased by 533 about +165 Gt/yr and ne30pg2 by +230 Gt/yr.

534 The combined annual snow/ice melt shown in the bottom panel of Figure 10 in- 535 dicates that the Arctic grid simulates the most realistic melt rates, with the other grids 536 having more melt than RACMO. The Arctic–GrIS grid over-predicts melting by about 537 125 Gt/yr. This is likely due to an anomalously warm lower troposphere during the sum- 538 mer, relative to the Arctic run (Figure 6). The f19 and f09 melting rates are improved 539 over Arctic–GrIS, overestimating melt by only 70–90 Gt/yr. The SE grids have the 540 largest positive melt bias, between 200–220 Gt/yr.

To illustrate the regional behavior of the SMB components, Figure 11 shows the precipitation and combined snow/ice melt integrated over the basins defined by Rignot and Mouginot (2012). The uncertainty due to differences in basin area is larger than for GrIS-wide integrals, owing to the differences in basin boundaries on the common ice masks, which are shown in the f19 and ne30pg2 panels of Figure 9. Nonetheless, the regional totals in Figure 11 correctly show the southeast and southwest basins have the most accumulation. In all basins, accumulation decreases monotonically with increasing grid resolution, though with some exceptions. The **Arctic–GrIS** grid simulates less precipitation than RACMO in the central-east and southeast basins, and is closest of all grids to RACMO in the large southwest basin.

The basin-integrated melt rates in Figure 11 depend on the dycore. The uniform-resolution SE grids have the largest positive biases in all basins. The **Arctic–GrIS** grid is a close second, while the FV grids have systematically smaller melt-rates. The “second-place” standing of **Arctic–GrIS** is somewhat unexpected, as this grid has the warmest lower-troposphere summer temperatures (Figure 6) and greatest incident shortwave radiation (Figure 8), yet it has less melting than the uniform-resolution SE grids.

Lower troposphere temperature is not a strict proxy for melting; e.g., it may not capture microclimate effects as a result of a better representation of the low-elevation ablation zones. The Positive Degree-Day temperature-based melt index (PDD; Braithwaite, 1984), which accumulates the near-surface temperature in $^{\circ}\text{C}$ for days with temperature above freezing, is a more accurate proxy for melting. PDD is nonlinear in mean monthly temperature (Reeh, 1991). We compute PDD from monthly mean 2-meter temperature using the method of Calov and Greve (2005), assuming a fixed monthly mean standard deviation of 3°C and a degree-day factor of $5 \text{ mm d}^{-1} ^{\circ}\text{C}^{-1}$.

Figure 11c shows the basin-integrated PDD melt estimate. In the large southeast and southwest basins (and all the other western basins), the ne30pg3 grid has larger PDD-based melt than the **Arctic–GrIS** grid. The FV grids also have large PDD-based melt in the southwest basin, relative to **Arctic–GrIS**. The PDD plots indicate that the relationship between temperature and melt is not well approximated by the summer lower-troposphere temperatures in Figure 6.

The bottom panel of Figure 9 presents the biases in the combined ice/snow melt as map plots. These plots show that the largest melt biases are on the southeast and northwest coasts, where large coarse-grid cells overlap with the ocean. One possibility is that these problematic grid cells are situated at lower elevations than the true ice sheet surface, leading to a warm bias and too much melt. Figure 12 shows the representation of the ice sheet surface along two transects on the different grids, compared to the high-resolution dataset used to generate CAM topographic boundary conditions (J. Danielson & Gesch, 2011; Lauritzen et al., 2015). The two transects are shown in Figure 9: the east-west “K-transect” in southwest Greenland and a transect extending from the central dome down to the Kangerlussuaq glacier on the southeast coast. The 1° – 2° grids are noticeably coarse, with only a handful of grid cells populating the transect. The f09 grid is a bit of an exception since the grid cells narrow in the zonal direction at high latitudes, and so a larger number of grid cells fit into the east-west transects. The VR grids more accurately reproduce the steep margins of the ice sheet, capturing the characteristic parabolic shape of the GrIS margin.

The transects in Figure 12 show that the ice sheet surface on the coarse grids is not systematically lower than the true surface in ablation zones. Rather, the smoothing and flattening of the raw topography, necessary to prevent the model from exciting grid-scale numerical modes, causes the lower-elevation ablation zones to extend beyond the true ice sheet margin, causing the modeled ablation zones (which must reside within the ice sheet mask) to be elevated relative to the actual ice surface. The f19 grid has both the smoothest topography and the flattest ice sheet since its dynamics are coars-

593 est, whereas the f09, ne30pg2 and ne30pg3 grids have similar dynamical resolution and
 594 use identical smoothing. This suggests that coarser models will tend to elevate the ab-
 595 lation zones and thereby depress melt rates, which is the opposite of the melt bias that
 596 occurs in the coarse grid simulations.

597 Figure 12 also shows the ice margin boundary, illustrating that the ablation zone
 598 lies in a narrow horizontal band where the ice sheet rapidly plunges to sea-level. Due to
 599 this abrupt transition, coarse grids will commonly represent the ablation zone with grid
 600 cells containing mixtures of ice-covered and ice-free regions. We hypothesize that coarser
 601 models have larger melt biases because summer melting is confined to these mixed ice/land/ocean
 602 grid cells. CLM deals with land heterogeneity in a complex and sophisticated manner,
 603 but CAM only sees the homogenized state after volume averaging over the sub-grid mix-
 604 ture. Thus, warm ice-free land patches in a grid cell may unduly influence the climate
 605 over the entire grid cell, causing a warm bias over the ice-covered patch.

606 Figure 13 shows the mean melt bias, relative to both RACMO datasets, condition-
 607 ally sampled based on grid cell ice fraction in the GrIS region. Errors are computed af-
 608 ter mapping the melt rates to the common ice masks using different methods, described
 609 in section 2.6. The grid cell ice fractions therefore pertain to ice fractions on the low-
 610 resolution common ice masks. Also shown are the ± 1 standard deviation of the biases
 611 for each bin. The figure shows that coarser grids can be characterized by a monotonic
 612 increase in melt bias as the grid cell ice fraction decreases. The VR grids have the small-
 613 est melt biases for small grid cell ice fractions (smaller than 50%), the uniform SE grids
 614 and f19 have the largest melt biases and the f09 grid melt biases lie between these two
 615 cases. Figure 13 generally supports our hypothesis that the prevalence of mixed-grid cells
 616 in the ablation zone of coarse grids is responsible for their large melt bias.

617 3.4 Precipitation extremes

618 Synoptic storms are tracked using TempestExtremes atmospheric feature detec-
 619 tion software (Ullrich et al., 2021). As the Arctic grid contains $1/4^\circ$ refinement north
 620 of about 45° latitude, the storm tracker is applied to this region for the Arctic and ne30pg3
 621 runs to identify differences in storm characteristics due to horizontal resolution.

622 Figure 14 shows monthly PDFs of the precipitation rates associated with storms.
 623 The PDFs are constructed by sampling all the precipitation rates within 30° of the storm
 624 center, for each point on the storm track and for all storms. The PDFs are evaluated on
 625 an identical composite grid for all runs, and so storm statistics are not impacted by dif-
 626 ferences in output resolution. The Arctic run has larger extreme precipitation rates com-
 627 pared to ne30pg3 in every month, but the increase is greatest in the summer months,
 628 which coincides with the most extreme events of the year. This is primarily due to in-
 629 creased resolution and not the reduced physics time step; the ne30pg3* run only marginally
 630 increases the extreme precipitation rates compared with ne30pg3 (Figure 14).

631 The extreme precipitation rates in the Arctic run are closer than ne30pg3 to the
 632 ERA5 reanalysis (Figure 14). It is difficult to know how much the extreme precipitation
 633 rates in ERA5 are constrained by data assimilation, or whether these precipitation rates
 634 are due to using a similar $1/4^\circ$ model as the Arctic grid. However, it is well documented
 635 that $1/4^\circ$ models are more skillful at simulating extreme events (Bacmeister et al., 2013;
 636 Obrien et al., 2016). A more realistic representation of extreme precipitation events is
 637 an additional benefit of the VR grids.

638 4 Conclusions

639 Running CESM2.2 in an AMIP-style configuration, we have evaluated six grids from
 640 two dynamical cores for their performance over the Arctic and in simulating the GrIS

641 SMB. The $1 - 2^\circ$ finite-volume grids have enhanced resolution over polar regions due
 642 to their convergence of meridian lines, although a polar filter is used to prevent spuri-
 643 ous atmospheric features from forming in these regions. SE grids comparable to the res-
 644 olution of the FV grids have an isotropic grid structure where the grid resolution is sim-
 645 ilar over the entire model domain. We developed two VR grids and introduced them into
 646 CESM2.2 as part of this work. Both use the SE dycore; the **Arctic** grid has $1/4^\circ$ refine-
 647 ment over the broader Arctic, whereas the **Arctic – GrIS** grid is identical except for
 648 a $1/8^\circ$ patch of refinement over Greenland. A third VR grid, **CONUS**, has also been made
 649 available in CESM2.2.

650 In general, the FV grids have colder summer temperatures over the Arctic com-
 651 pared with the SE grids (including the VR grids). The cloud biases in all the uniform-
 652 resolution grids, whether FV or SE, are similar, in general being too cloudy over Arc-
 653 tic land masses. It should be emphasized that our analysis is specific to the Arctic sum-
 654 mer because of its relevance to GrIS melt rates. An improved representation of clouds
 655 in the Arctic does not imply improved clouds at lower latitudes.

656 At the regional level, there is a halo of negative cloudiness bias around the ocean
 657 perimeter of Greenland on all $1 - 2^\circ$ grids, but not the VR grids. This negative cloud
 658 bias contrasts with a positive cloud bias over the ice sheet interior. This anomaly pat-
 659 tern is attributed to deficient orographic precipitation in the coarser model grids. With
 660 overly smooth topography on the $1 - 2^\circ$ grids, synoptic systems moving into Greenland
 661 are not sufficiently lifted when encountering the steep ice margins. As a result, excess
 662 precipitation falls in the GrIS interior, instead of being concentrated on the steep coastal
 663 margins as shown by observations (Pollard & Groups, 2000; van Kampenhout et al., 2018).
 664 This results in a positive precipitation and cloud bias in the ice sheet interior, and a halo
 665 of low cloud bias about the perimeter. The agreement of different observational data prod-
 666 ucts on this bias lends confidence in the attribution of causes. The VR grids compare
 667 better to the observations and show that orographic precipitation in Greenland is largely
 668 resolved when the horizontal resolution is increased sufficiently.

669 We integrated the primary source and sink terms of the SMB equation over the GrIS
 670 for each of the six grids. The uniform $1^\circ - 2^\circ$ grids have large positive accumulation bi-
 671 ases because they fail to resolve orographic precipitation. The uniform SE grids have larger
 672 accumulation biases, suggesting that the FV grids are more skillful for precipitation due
 673 to finer resolution over Greenland, and despite a polar filter. The VR grids have the most
 674 accurate accumulation rates of all the grids. The primary mass sink term of the GrIS,
 675 ice/snow melt, has similar biases; the coarse grids melt too much, with a greater bias for
 676 uniform SE grids. In general, on coarse grids, errors in the individual SMB terms are larger
 677 than the errors in the SMB itself, due to compensating errors. This observation serves
 678 as a precaution; projecting mass-loss from a glacier or ice sheet cannot be reliable if the
 679 processes representing the components of the SMB are incorrect from the start, even if
 680 the total SMB has the right magnitude.

681 The **Arctic – GrIS** grid has the warmest summer lower troposphere of all grids,
 682 yet it has less melting than the uniform-resolution SE grids. This suggests that grid res-
 683 olution is somehow contributing to the melt biases in coarse grids, in a way that is not
 684 obvious from the large-scale dynamics. We propose a mechanism: coarse grids represent
 685 ablation zones using grid cells with mixed surface types, ice-covered and ice-free. The
 686 warmer ice-free patches may largely determine the mean state, leading to a warm bias
 687 over the ice-covered patches of the grid cell. This mechanism is supported by analysis
 688 of melt biases binned by grid-cell ice fraction.

689 The **Arctic** grid substantially improves the simulated Arctic climate, including pre-
 690 cipitation extremes and the GrIS SMB, compared to the uniform $1^\circ - 2^\circ$ grids. The **Arctic –**
 691 **GrIS** grid has the most realistic cloud and precipitation fields, but its summer temper-
 692 atures are too warm. The 1° FV model gives a surprisingly realistic SMB, likely due to

the relatively fine resolution of Greenland on lat-lon grids (but perhaps also because it is the most heavily tuned model configuration in CESM). In particular, a greater number of grid cells in the ablation zone reduces the influence of mixed ice-covered/ice-free grid cells that represent ablation poorly on the other uniform-resolution grids.

As modeling systems move away from lat-lon grids towards quasi-uniform unstructured grids, it is worth taking stock of whether this will degrade the simulated polar climate. We have found that the 1° FV model has clear advantages over the 1° SE model for simulating the GrIS SMB. That is, the simulated GrIS SMB will be adversely impacted in future CESM versions, after the FV dycore is phased out. This finding will not interrupt the ongoing transition towards unstructured grids in CESM, which is largely driven by gains in computational efficiency and grid refinement capabilities. We therefore provide the Arctic refined-meshes to the community by way of CESM2.2, providing users the option to simulate a more realistic GrIS SMB, although at a substantial computational premium relative to conventional 1° – 2° grids.

We are working to develop a configuration of the **Arctic** grid that is fully-coupled with the CESM ocean and sea ice components and the Community Ice Sheet Model (CISM), to provide multi-century projections of the state of the GrIS and its contribution to sea-level rise. We have also developed a visualization of the **Arctic–GrIS** run, now available on youtube (see link in Acknowledgements) to increase awareness of the capabilities of CESM2.2. Figure 15 shows a snapshot of this visualization, illustrating mesoscale katabatic winds descending the southeastern slopes of the GrIS. These new grids and configurations will provide new opportunities for CESM polar science, and they aim to contribute to an improved understanding of the polar environment. However, we recognize the potentially prohibitive costs for some users, and so will continue to explore different grids, parameterizations and workflows that can provide some of the same benefits of the VR grids, but at a lower cost.

719 **Appendix A Details on spectra-element dynamical core improvements 720 since the CESM2.0 release**

721 Since the CESM2.0 release of the spectral-element dynamical core documented in
722 Lauritzen et al. (2018) some important algorithmic improvements have been implemented
723 and released with CESM2.2. These pertain mainly to the flow over orography that, for
724 the spectral-element dynamical core, can lead to noise aligned with the element bound-
725 aries (Herrington et al., 2018).

726 **A1 Reference profiles**

727 Significant improvement in removing noise for flow over orography can be achieved
728 by using reference profiles for temperature and pressure

$$T^{(ref)} = T_0 + T_1 \Pi^{(ref)}, \quad (A1)$$

$$p_s^{(ref)} = p_0 \exp\left(-\frac{\Phi_s}{R^{(d)} T_{ref}}\right), \quad (A2)$$

729 (Simmons & Jiabin, 1991) where g gravity, $T_1 = \Gamma_0 T_{ref} c_p^{(d)} / g \approx 192K$ with standard
730 lapse rate $\Gamma_0 \equiv 6.5K/km$ and $T_0 \equiv T_{ref} - T_1 \approx 97K$; $T_{ref} = 288K$ ($c_p^{(d)}$ specific heat
731 of dry air at constant pressure; $R^{(d)}$ gas constant for dry air), and Φ_s surface geopoten-
732 tial. The reference Exner function is

$$\Pi^{(ref)} = \left(\frac{p^{(ref)}}{p_0}\right)^\kappa \quad (A3)$$

733 where $\kappa = \frac{R^{(d)}}{c_p^{(d)}}$. The reference surface pressure $p_0 = 1000\text{hPa}$ and at each model level
 734 the reference pressure $p^{(ref)}$ is computed from $p_s^{(ref)}$ and the standard hybrid coefficients

$$p^{(ref)}(\eta) = A(\eta)p_0 + B(\eta)p_s^{(ref)}, \quad (\text{A4})$$

735 where A and B are the standard hybrid coefficients (using a dry-mass generalized ver-
 736 tical mass coordinate η). These reference profiles are subtracted from the prognostic tem-
 737 perature and pressure-level-thickness states before applying hyperviscosity:

CESM2.0 → CESM2.2

$$\nabla_\eta^4 T \rightarrow \nabla_\eta^4 (T - T^{(ref)}), \quad (\text{A5})$$

$$\nabla_\eta^4 \delta p^{(d)} \rightarrow \nabla_\eta^4 (\delta p^{(d)} - \delta p^{(ref)}). \quad (\text{A6})$$

738 This reduces spurious transport of temperature and mass up/down-slope due to the hy-
 739 perviscosity operator.

740 A2 Rewriting the pressure gradient force (PGF)

741 In the CESM2.0 the following (standard) form of the pressure gradient term was
 742 used:

$$\nabla_\eta \Phi + \frac{1}{\rho} \nabla_\eta p, \quad (\text{A7})$$

743 where Φ is geopotential and $\rho = \frac{R^{(d)} T_v}{p}$ is density (for details see Lauritzen et al., 2018).
 744 To alleviate noise for flow over orography, we switched to an Exner pressure formulation
 745 following Taylor et al. (2020), which uses that (A7) can be written in terms of the Exner
 746 pressure

$$\nabla_\eta \Phi + c_p^{(d)} \theta_v \nabla_\eta \Pi, \quad (\text{A8})$$

747 where the Exner pressure is

$$\Pi \equiv \left(\frac{p}{p_0} \right)^\kappa. \quad (\text{A9})$$

748 The derivation showing that (A7) and (A8) are equivalent is shown here:

$$\begin{aligned} c_p^{(d)} \theta_v \nabla_\eta \Pi &= c_p^{(d)} \theta_v \nabla_\eta \left(\frac{p}{p_0} \right)^\kappa, \\ &= c_p^{(d)} \theta_v \kappa \left(\frac{p}{p_0} \right)^{\kappa-1} \nabla_\eta \left(\frac{p}{p_0} \right), \\ &= c_p^{(d)} \theta_v \kappa \Pi \left(\frac{p_0}{p} \right) \nabla_\eta \left(\frac{p}{p_0} \right), \\ &= \frac{c_p^{(d)} \theta_v \kappa \Pi}{p} \nabla_\eta p, \\ &= \frac{R^{(d)} \theta_v \Pi}{p} \nabla_\eta p, \\ &= \frac{R^{(d)} T_v}{p} \nabla_\eta p, \\ &= \frac{1}{\rho} \nabla_\eta p. \end{aligned}$$

749 Using the reference states from (Simmons & Jiabin, 1991),

$$\bar{T} = T_0 + T_1 \Pi, \quad (\text{A10})$$

$$\bar{\theta} = T_0 / \Pi + T_1, \quad (\text{A11})$$

750 we can define a geopotential as a function of Exner pressure

$$\bar{\Phi} = -c_p^{(d)} (T_0 \log \Pi + T_1 \Pi - T_1). \quad (\text{A12})$$

751 This "balanced" geopotential obeys

$$c_p^{(d)} \bar{\theta} \nabla \Pi + \nabla \bar{\Phi} = 0 \quad (\text{A13})$$

752 for any Exner pressure. Subtracting this "reference" profile from the PGF yields

$$\begin{aligned} \nabla_\eta \Phi + c_p^{(d)} \theta_v \nabla_\eta \Pi &= \nabla_\eta (\Phi - \bar{\Phi}) + c_p^{(d)} (\theta_v - \bar{\theta}) \nabla_\eta \Pi, \\ &= \nabla_\eta \Phi + c_p^{(d)} \theta_v \nabla_\eta \Pi + c_p^{(d)} T_0 \left[\nabla_\eta \log \Pi - \frac{1}{\Pi} \nabla_\eta \Pi \right]. \end{aligned} \quad (\text{A14})$$

753 In the continuum, the two formulations (left and right-hand side of (A14)) are identical.
754 But under discretization, the second formulation can have much less truncation error.
755

756 A3 Results

757 One year averages of vertical pressure velocity at 500hPa (OMEGA500) have been
758 found to be a useful quantity to detect spurious up or down-drafts induced by steep orog-
759 raphy (Figure A1). While the true solution is not known, strong vertical velocities aligned
760 with element edges that are not found in the CAM-FV reference solution (Figure A1(a))
761 are likely not physical (spurious). The older CESM2.0 version of SE (Figure A1(d)) us-
762 ing the "traditional" discretization of the PGF, (A14), exhibits significant spurious noise
763 patters around steep orography compared to CAM-FV (e.g., around Himalayas and An-
764 des). This is strongly alleviated by switching to the Exner formulation of the PGF (A8;
765 Figure A1(c)). By also subtracting reference profiles from pressure-level thickness and
766 temperature, equations (A5) and (A6) respectively, reduces strong up-down drafts fur-
767 ther (Figure A1(d)). Switching to the CAM-SE-CSLAM version where physics ten-
768 dencies are computed on an quasi-equal area physics grid and using the CSLAM transport
769 scheme, marginal improvements are observed in terms of a smoother vertical velocity field
770 (Figure A1(e,f)). The configuration shown in Figure A1(d) is used for the simulations
771 shown in the main text of this paper.

772 It is interesting to note that the noise issues and algorithmic remedies found in the
773 real-world simulations discussed above, can be investigated by replacing all of physics
774 with a modified version of the Held-Suarez forcing (Held & Suarez, 1994). The original
775 formulation of the Held-Suarez idealized test case used a flat Earth ($\Phi_s = 0$) and a dry
776 atmosphere. By simply adding the surface topography used in 'real-world' simulations
777 and removing the temperature relaxation in the lower part of domain ($\sigma > 0.7$; see Held
778 and Suarez (1994) for details), surprisingly realistic vertical velocity fields (in terms of
779 structure) result (see Figure A2). Since this was a very useful development tool it is shared
780 in this manuscript.

781 Acknowledgments

782 This material is based upon work supported by the National Center for Atmospheric Re-
783 search (NCAR), which is a major facility sponsored by the NSF under Cooperative Agree-
784 ment 1852977. Computing and data storage resources, including the Cheyenne super-
785 computer (doi:10.5065/D6RX99HX), were provided by the Computational and Informa-
786 tion Systems Laboratory (CISL) at NCAR. A. Herrington thanks Matt Rehme (NCAR/CISL)
787 for his role in generating the Arctic-GrIS visualization available on youtube (https://www.youtube.com/watch?v=YwHgqDu75s8&t=4s&ab_channel=NCARVisLab).
788

789 The data presented in main part of this manuscript is available at <https://github.com/adamrher/2020-arcticgrids>. The source code and data for the Appendix is avail-
790 able at <https://github.com/PeterHjortLauritzen/CAM/tree/topo-mods>.
791

792 References

- Bacmeister, J. T., & Coauthors. (2018). Projected changes in tropical cyclone activity under future warming scenarios using a high-resolution climate model. *Climatic Change*, 146, 547–560. Retrieved from <http://dx.doi.org/10.1007/s10584-016-1750-x> doi: 10.1007/s10584-016-1750-x
- Bacmeister, J. T., Wehner, M. F., Neale, R. B., Gettelman, A., Hannay, C., Lautzen, P. H., ... Truesdale, J. E. (2013). Exploratory high-resolution climate simulations using the community atmosphere model (cam). *J. Climate*, 27(9), 3073–3099. doi: 10.1175/JCLI-D-13-00387.1
- Bambach, N. E., Rhoades, A. M., Hatchett, B. J., Jones, A. D., Ullrich, P. A., & Zarzycki, C. M. (2021). Projecting climate change in south america using variable-resolution community earth system model: An application to chile. *International Journal of Climatology*.
- Beljaars, A., Brown, A., & Wood, N. (2004). A new parametrization of turbulent orographic form drag. *Quart. J. Roy. Meteor. Soc.*, 130(599), 1327–1347. doi: 10.1256/qj.03.73
- Bogenschutz, P. A., Gettelman, A., Morrison, H., Larson, V. E., Craig, C., & Schanen, D. P. (2013). Higher-order turbulence closure and its impact on climate simulations in the community atmosphere model. *Journal of Climate*, 26(23), 9655–9676.
- Box, J. E., Bromwich, D. H., & Bai, L.-S. (2004). Greenland ice sheet surface mass balance 1991–2000: Application of polar mm5 mesoscale model and in situ data. *Journal of Geophysical Research: Atmospheres*, 109(D16).
- Braithwaite, R. J. (1984). Calculation of degree-days for glacier-climate research. *Zeitschrift für Gletscherkunde und Glazialgeologie*, 20(1984), 1–8.
- Burakowski, E. A., Tawfik, A., Ouimette, A., Lepine, L., Zarzycki, C., Novick, K., ... Bonan, G. (2019). Simulating surface energy fluxes using the variable-resolution community earth system model (vr-cesm). *Theoretical and Applied Climatology*, 138(1), 115–133.
- Calov, R., & Greve, R. (2005). A semi-analytical solution for the positive degree-day model with stochastic temperature variations. *Journal of Glaciology*, 51(172), 173–175.
- Canuto, C., Hussaini, M. Y., Quarteroni, A., & Zang, T. (2007). *Spectral methods: Evolution to complex geometries and applications to fluid dynamics* (1st ed.). Springer.
- Chang, P., Zhang, S., Danabasoglu, G., Yeager, S. G., Fu, H., Wang, H., ... others (2020). An unprecedented set of high-resolution earth system simulations for understanding multiscale interactions in climate variability and change. *Journal of Advances in Modeling Earth Systems*, 12(12), e2020MS002298.
- Chepfer, H., Bony, S., Winker, D., Cesana, G., Dufresne, J., Minnis, P., ... Zeng, S. (2010). The gcm-oriented calipso cloud product (calipso-goccp). *Journal of Geophysical Research: Atmospheres*, 115(D4).
- Collins, W. D., Rasch, P. J., Boville, B. A., Hack, J. J., McCaa, J. R., Williamson, D. L., ... Zhang, M. (2006). The formulation and atmospheric simulation of the community atmosphere model version 3 (cam3). *Journal of Climate*, 19(11), 2144–2161.
- Copernicus, C. (2019). Era5 monthly averaged data on pressure levels from 1979 to present. URL: <https://cds.climate.copernicus.eu>. doi: 10.24381/cds.6860a573
- Craig, C., Bacmeister, J., Callaghan, P., Eaton, B., Gettelman, A., Goldhaber, S. N., ... Vitt, F. M. (2021). *Cam6.3 user's guide* (Tech. Rep.). NCAR/TN-571+EDD. doi: 10.5065/Z953-ZC95
- Danabasoglu, G., Lamarque, J.-F., Bacmeister, J., Bailey, D., DuVivier, A., Edwards, J., ... others (2020). The community earth system model ver-

- 846 sion 2 (cesm2). *Journal of Advances in Modeling Earth Systems*, 12(2),
 847 e2019MS001916.
- 848 Danielson, J., & Gesch, D. (2011). *Global multi-resolution terrain elevation data*
 849 *2010 (GMTED2010)* (Open-File Report 2011-1073). U.S. Geological Survey.
 850 (<http://pubs.usgs.gov/of/2011/1073/pdf/of2011-1073.pdf>)
- 851 Danielson, J. J., & Gesch, D. B. (2011). *Global multi-resolution terrain elevation*
 852 *data 2010 (GMTED2010)* (Open File Rep. No. 2011-1073). US Geological Sur-
 853 vey. doi: <https://doi.org/10.3133/ofr20111073>
- 854 Dennis, J. M., Edwards, J., Evans, K. J., Guba, O., Lauritzen, P. H., Mirin, A. A.,
 855 ... Worley, P. H. (2012). CAM-SE: A scalable spectral element dynamical
 856 core for the Community Atmosphere Model. *Int. J. High. Perform. C.*, 26(1),
 857 74–89. Retrieved from <http://hpc.sagepub.com/content/26/1/74.abstract>
 858 doi: 10.1177/1094342011428142
- 859 Evans, K. J., Kennedy, J. H., Lu, D., Forrester, M. M., Price, S., Fyke, J., ... oth-
 860 ers (2019). Livvkit 2.1: automated and extensible ice sheet model validation.
 861 *Geoscientific Model Development*, 12(3), 1067–1086.
- 862 Eyring, V., Bony, S., Meehl, G. A., Senior, C. A., Stevens, B., Stouffer, R. J., &
 863 Taylor, K. E. (2016). Overview of the coupled model intercomparison project
 864 phase 6 (cmip6) experimental design and organization. *Geoscientific Model*
 865 *Development*, 9(5), 1937–1958.
- 866 Fettweis, X., Franco, B., Tedesco, M., Van Angelen, J., Lenaerts, J. T., van den
 867 Broeke, M. R., & Gallée, H. (2013). Estimating the greenland ice sheet
 868 surface mass balance contribution to future sea level rise using the regional
 869 atmospheric climate model mar. *The Cryosphere*, 7(2), 469–489.
- 870 Gettelman, A., Callaghan, P., Larson, V., Zarzycki, C., Bacmeister, J., Lauritzen, P.,
 871 ... Neale, R. (2017). Regional climate simulations with the community earth
 872 system model. *J. Adv. Model. Earth Syst.*. (submitted)
- 873 Gettelman, A., Hannay, C., Bacmeister, J. T., Neale, R. B., Pendergrass, A., Dan-
 874 abasoglu, G., ... others (2019). High climate sensitivity in the community
 875 earth system model version 2 (cesm2). *Geophysical Research Letters*, 46(14),
 876 8329–8337.
- 877 Gettelman, A., & Morrison, H. (2015). Advanced two-moment bulk microphysics for
 878 global models. part i: Off-line tests and comparison with other schemes. *Jour-*
 879 *nal of Climate*, 28(3), 1268–1287.
- 880 Gettelman, A., Morrison, H., Santos, S., Bogsenschutz, P., & Caldwell, P. (2015).
 881 Advanced two-moment bulk microphysics for global models. part ii: Global
 882 model solutions and aerosol–cloud interactions. *Journal of Climate*, 28(3),
 883 1288–1307.
- 884 Golaz, J.-C., Larson, V. E., & Cotton, W. R. (2002). A pdf-based model for bound-
 885 ary layer clouds. part i: Method and model description. *Journal of the Atmo-*
 886 *spheric Sciences*, 59(24), 3540–3551. doi: 10.1175/1520-0469(2002)059<3540:
- 887 apbmfb>2.0.co;2
- 888 Guba, O., Taylor, M. A., Ullrich, P. A., Overfelt, J. R., & Levy, M. N. (2014). The
 889 spectral element method (sem) on variable-resolution grids: evaluating grid
 890 sensitivity and resolution-aware numerical viscosity. *Geosci. Model Dev.*, 7(6),
 891 2803–2816. doi: 10.5194/gmd-7-2803-2014
- 892 Guo, Z., Wang, M., Qian, Y., Larson, V. E., Ghan, S., Ovchinnikov, M., ... Zhou,
 893 T. (2015). Parametric behaviors of clubb in simulations of low clouds in the c
 894 omunity atmosphere m odel (cam). *Journal of Advances in Modeling Earth*
 895 *Systems*, 7(3), 1005–1025.
- 896 Hansen, N., Simonsen, S. B., Boberg, F., Kittel, C., Orr, A., Souverijns, N., ... Mot-
 897 tram, R. (2022). Brief communication: Impact of common ice mask in surface
 898 mass balance estimates over the antarctic ice sheet. *The Cryosphere*, 16(2),
 899 711–718.
- 900 Held, I. M., & Suarez, M. J. (1994). A proposal for the intercomparison of the dy-

- namical cores of atmospheric general circulation models. *Bull. Am. Meteorol. Soc.*, 73, 1825–1830.
- Herrington, A. R., Lauritzen, P., Taylor, M. A., Goldhaber, S., Eaton, B. E., Bacmeister, J., ... Ullrich, P. (2018). Physics-dynamics coupling with element-based high-order galerkin methods: quasi equal-area physics grid. *Mon. Wea. Rev.*, 47, 69–84. doi: 10.1175/MWR-D-18-0136.1
- Herrington, A. R., Lauritzen, P. H., Reed, K. A., Goldhaber, S., & Eaton, B. E. (2019). Exploring a lower resolution physics grid in cam-se-cslam. *Journal of Advances in Modeling Earth Systems*, 11.
- Herrington, A. R., & Reed, K. A. (2018). An idealized test of the response of the community atmosphere model to near-grid-scale forcing across hydrostatic resolutions. *J. Adv. Model. Earth Syst.*, 10(2), 560–575.
- Herrington, A. R., & Reed, K. A. (2020). On resolution sensitivity in the community atmosphere model. *Quarterly Journal of the Royal Meteorological Society*, 146(733), 3789–3807.
- Hurrell, J. W., Hack, J. J., Shea, D., Caron, J. M., & Rosinski, J. (2008). A new sea surface temperature and sea ice boundary dataset for the community atmosphere model. *Journal of Climate*, 21(19), 5145–5153.
- Jablonowski, C., & Williamson, D. L. (2011). The pros and cons of diffusion, filters and fixers in atmospheric general circulation models. In P. H. Lauritzen, C. Jablonowski, M. Taylor, & R. Nair (Eds.), *Numerical techniques for global atmospheric models* (pp. 381–493). Berlin, Heidelberg: Springer Berlin Heidelberg. doi: 10.1007/978-3-642-11640-7_13
- Lauritzen, P. H., Bacmeister, J. T., Callaghan, P. F., & Taylor, M. A. (2015). Ncar global model topography generation software for unstructured grids. *Geoscientific Model Development Discussions*, 8(6), 4623–4651. doi: 10.5194/gmdd-8-4623-2015
- Lauritzen, P. H., Jablonowski, C., Taylor, M., & Nair, R. D. (2010). Rotated versions of the jablonowski steady-state and baroclinic wave test cases: A dynamical core intercomparison. *J. Adv. Model. Earth Syst.*, 2(15), 34 pp.
- Lauritzen, P. H., Mirin, A., Truesdale, J., Raeder, K., Anderson, J., Bacmeister, J., & Neale, R. B. (2011). Implementation of new diffusion/filtering operators in the CAM-FV dynamical core. *Int. J. High Perform. Comput. Appl.*. doi: 10.1177/1094342011410088
- Lauritzen, P. H., Nair, R., Herrington, A., Callaghan, P., Goldhaber, S., Dennis, J., ... Dubos, T. (2018). NCAR release of CAM-SE in CESM2.0: A reformulation of the spectral-element dynamical core in dry-mass vertical coordinates with comprehensive treatment of condensates and energy. *J. Adv. Model. Earth Syst.*, 10(7), 1537–1570. doi: 10.1029/2017MS001257
- Lauritzen, P. H., Taylor, M. A., Overfelt, J., Ullrich, P. A., Nair, R. D., Goldhaber, S., & Kelly, R. (2017). CAM-SE-CSLAM: Consistent coupling of a conservative semi-lagrangian finite-volume method with spectral element dynamics. *Mon. Wea. Rev.*, 145(3), 833–855. doi: 10.1175/MWR-D-16-0258.1
- Lawrence, D. M., Fisher, R. A., Koven, C. D., Oleson, K. W., Swenson, S. C., Bonan, G., ... others (2019). The community land model version 5: Description of new features, benchmarking, and impact of forcing uncertainty. *Journal of Advances in Modeling Earth Systems*, 11(12), 4245–4287.
- Lin, S.-J. (2004). A 'vertically Lagrangian' finite-volume dynamical core for global models. *Mon. Wea. Rev.*, 132, 2293–2307.
- Lin, S.-J., & Rood, R. B. (1997). An explicit flux-form semi-Lagrangian shallow-water model on the sphere. *Q.J.R.Meteorol.Soc.*, 123, 2477–2498.
- Lipscomb, W. H., Fyke, J. G., Vizcaíno, M., Sacks, W. J., Wolfe, J., Vertenstein, M., ... Lawrence, D. M. (2013). Implementation and initial evaluation of the glimmer community ice sheet model in the community earth system model. *Journal of Climate*, 26(19), 7352–7371.

- 956 Loeb, N. G., Doelling, D. R., Wang, H., Su, W., Nguyen, C., Corbett, J. G., ...
 957 Kato, S. (2018). Clouds and the earth's radiant energy system (ceres) energy
 958 balanced and filled (ebaf) top-of-atmosphere (toa) edition-4.0 data product.
 959 *Journal of Climate*, 31(2), 895–918.
- 960 Lofverstrom, M., Fyke, J. G., Thayer-Calder, K., Muntjewerf, L., Vizcaino, M.,
 961 Sacks, W. J., ... Bradley, S. L. (2020). An efficient ice sheet/earth sys-
 962 tem model spin-up procedure for cesm2-cism2: Description, evaluation, and
 963 broader applicability. *Journal of Advances in Modeling Earth Systems*, 12(8),
 964 e2019MS001984.
- 965 Mottram, R., Boberg, F., Langen, P., Yang, S., Rodehacke, C., Christensen, J. H.,
 966 & Madsen, M. S. (2017). Surface mass balance of the greenland ice sheet in
 967 the regional climate model hirham5: Present state and future prospects. *Low
 968 Temp. Sci.*, 75, 105–115.
- 969 Muntjewerf, L., Sacks, W. J., Lofverstrom, M., Fyke, J., Lipscomb, W. H., Er-
 970 nani da Silva, C., ... Sellevold, R. (2021). Description and Demonstration of
 971 the Coupled Community Earth System Model v2–Community Ice Sheet Model
 972 v2 (CESM2-CISM2). *Journal of Advances in Modeling Earth Systems*, 13(6),
 973 e2020MS002356.
- 974 Neale, R. B., Richter, J. H., & Jochum, M. (2008). The impact of convection on
 975 ENSO: From a delayed oscillator to a series of events. *J. Climate*, 21, 5904-
 976 5924.
- 977 Noël, B., Van De Berg, W., Van Meijgaard, E., Kuipers Munneke, P., Van De Wal,
 978 R., & Van Den Broeke, M. (2015). Evaluation of the updated regional climate
 979 model racmo2. 3: summer snowfall impact on the greenland ice sheet. *The
 980 Cryosphere*, 9(5), 1831–1844.
- 981 Noël, B., van de Berg, W. J., Lhermitte, S., & van den Broeke, M. R. (2019). Rapid
 982 ablation zone expansion amplifies north greenland mass loss. *Science advances*,
 983 5(9), eaaw0123.
- 984 Noël, B., van de Berg, W. J., Van Wessem, J. M., Van Meijgaard, E., Van As, D.,
 985 Lenaerts, J., ... others (2018). Modelling the climate and surface mass bal-
 986 ance of polar ice sheets using racmo2–part 1: Greenland (1958–2016). *The
 987 Cryosphere*, 12(3), 811–831.
- 988 Obrien, T. A., Collins, W. D., Kashinath, K., Rübel, O., Byna, S., Gu, J., ...
 989 Ullrich, P. A. (2016). Resolution dependence of precipitation statistical
 990 fidelity in hindcast simulations. *J. Adv. Model. Earth Syst.*, 8(2), 976–
 991 990. Retrieved from <http://dx.doi.org/10.1002/2016ms000671> doi:
 992 10.1002/2016ms000671
- 993 Ohmura, A. (2001). Physical basis for the temperature-based melt-index method.
 994 *Journal of applied Meteorology*, 40(4), 753–761.
- 995 Pfister, G. G., Eastham, S. D., Arellano, A. F., Aumont, B., Barsanti, K. C., Barth,
 996 M. C., ... others (2020). The multi-scale infrastructure for chemistry and
 997 aerosols (musica). *Bulletin of the American Meteorological Society*, 101(10),
 998 E1743–E1760.
- 999 Pollard, D. (2010). A retrospective look at coupled ice sheet–climate modeling. *Cli-
 1000 matic Change*, 100(1), 173–194.
- 1001 Pollard, D., & Groups, P. P. (2000). Comparisons of ice-sheet surface mass budgets
 1002 from paleoclimate modeling intercomparison project (pmip) simulations. *Global
 1003 and Planetary Change*, 24(2), 79–106.
- 1004 Pope, V., & Stratton, R. (2002). The processes governing horizontal resolution sensi-
 1005 tivity in a climate model. *Climate Dynamics*, 19(3-4), 211–236.
- 1006 Putman, W. M., & Lin, S.-J. (2007). Finite-volume transport on various cubed-
 1007 sphere grids. *J. Comput. Phys.*, 227(1), 55–78.
- 1008 Rae, J., Adalgeirsdóttir, G., Edwards, T. L., Fettweis, X., Gregory, J., Hewitt, H.,
 1009 ... others (2012). Greenland ice sheet surface mass balance: evaluating simu-
 1010 lations and making projections with regional climate models. *The Cryosphere*,

- 1011 6(6), 1275–1294.
- 1012 Rasch, P. J., & Williamson, D. L. (1990). Computational aspects of moisture trans-
1013 port in global models of the atmosphere. *Q. J. R. Meteorol. Soc.*, 116, 1071-
1014 1090.
- 1015 Reeh, N. (1991). Parameterization of melt rate and surface temperature in the
1016 greenland ice sheet. *Polarforschung*, 59(3), 113–128.
- 1017 Rhoades, A. M., Huang, X., Ullrich, P. A., & Zarzycki, C. M. (2016). Characterizing
1018 sierra nevada snowpack using variable-resolution cesm. *Journal of Applied Me-
1019 teorology and Climatology*, 55(1), 173-196. Retrieved from <https://doi.org/10.1175/JAMC-D-15-0156.1> doi: 10.1175/JAMC-D-15-0156.1
- 1020 Richter, J. H., Sassi, F., & Garcia, R. R. (2010). Toward a physically based gravity
1021 wave source parameterization in a general circulation model. *J. Atmos. Sci.*,
1022 67, 136-156. doi: dx.doi.org/10.1175/2009JAS3112.1
- 1023 Rignot, E., & Mouginot, J. (2012). Ice flow in greenland for the international polar
1024 year 2008–2009. *Geophysical Research Letters*, 39(11).
- 1025 Roeckner, E., Brokopf, R., Esch, M., Giorgetta, M., Hagemann, S., Kornblueh, L.,
1026 ... Schulzweida, U. (2006). Sensitivity of simulated climate to horizontal
1027 and vertical resolution in the echam5 atmosphere model. *Journal of Climate*,
1028 19(16), 3771–3791.
- 1029 Sellevold, R., Van Kampenhout, L., Lenaerts, J., Noël, B., Lipscomb, W. H., &
1030 Vizcaino, M. (2019). Surface mass balance downscaling through elevation
1031 classes in an earth system model: Application to the greenland ice sheet. *The
1032 Cryosphere*, 13(12), 3193–3208.
- 1033 Serreze, M. C., Barrett, A. P., Slater, A. G., Steele, M., Zhang, J., & Trenberth,
1034 K. E. (2007). The large-scale energy budget of the arctic. *Journal of Geophys-
1035 ical Research: Atmospheres*, 112(D11).
- 1036 Simmons, A. J., & Jiabin, C. (1991). The calculation of geopotential and
1037 the pressure gradient in the ECMWF atmospheric model: Influence on
1038 the simulation of the polar atmosphere and on temperature analyses.
1039 *Quart. J. Roy. Meteor. Soc.*, 117(497), 29–58. Retrieved from <https://rmetsonlinelibrary.wiley.com/doi/abs/10.1002/qj.49711749703> doi:
1040 <https://doi.org/10.1002/qj.49711749703>
- 1041 Small, R. J., Bacmeister, J., Bailey, D., Baker, A., Bishop, S., Bryan, F., ... Verten-
1042 stein, M. (2014). A new synoptic scale resolving global climate simulation
1043 using the community earth system model. *J. Adv. Model. Earth Syst.*, 6(4),
1044 1065–1094. doi: 10.1002/2014MS000363
- 1045 Suarez, M. J., & Takacs, L. L. (1995). Volume 5 documentation of the aries/geos dy-
1046 namical core: Version 2.
- 1047 Taylor, M. A., & Fournier, A. (2010). A compatible and conservative spectral el-
1048 ement method on unstructured grids. *J. Comput. Phys.*, 229(17), 5879 - 5895.
1049 doi: 10.1016/j.jcp.2010.04.008
- 1050 Taylor, M. A., Guba, O., Steyer, A., Ullrich, P. A., Hall, D. M., & Eldred, C.
1051 (2020). An energy consistent discretization of the nonhydrostatic equations
1052 in primitive variables. *Journal of Advances in Modeling Earth Systems*, 12(1).
1053 doi: 10.1029/2019MS001783
- 1054 Taylor, M. A., Tribbia, J., & Iskandarani, M. (1997). The spectral element method
1055 for the shallow water equations on the sphere. *J. Comput. Phys.*, 130, 92-108.
- 1056 Team, E. J. S., Balaji, V., Boville, B., Collins, N., Craig, T., Cruz, C., ... others
1057 (2021). *Esmf user guide* (Tech. Rep.).
- 1058 Ullrich, P. A., & Taylor, M. A. (2015). Arbitrary-order conservative and consis-
1059 tent remapping and a theory of linear maps: Part i. *Monthly Weather Review*,
1060 143(6), 2419–2440.
- 1061 Ullrich, P. A., Zarzycki, C. M., McClenney, E. E., Pinheiro, M. C., Stansfield, A. M.,
1062 & Reed, K. A. (2021). Tempestextremes v2. 1: a community framework for
1063 feature detection, tracking and analysis in large datasets. *Geoscientific Model
1064*

- 1066 *Development Discussions*, 1–37.
- 1067 Van Angelen, J., Lenaerts, J., Lhermitte, S., Fettweis, X., Kuipers Munneke, P.,
 1068 Van den Broeke, M., ... Smeets, C. (2012). Sensitivity of greenland ice
 1069 sheet surface mass balance to surface albedo parameterization: a study with a
 1070 regional climate model. *The Cryosphere*, 6(5), 1175–1186.
- 1071 van Kampenhout, L., Lenaerts, J. T., Lipscomb, W. H., Lhermitte, S., Noël, B.,
 1072 Vizcaíno, M., ... van den Broeke, M. R. (2020). Present-day greenland ice
 1073 sheet climate and surface mass balance in cesm2. *Journal of Geophysical
 1074 Research: Earth Surface*, 125(2).
- 1075 van Kampenhout, L., Rhoades, A. M., Herrington, A. R., Zarzycki, C. M., Lenaerts,
 1076 J. T. M., Sacks, W. J., & van den Broeke, M. R. (2018). Regional grid refine-
 1077 ment in an earth system model: Impacts on the simulated greenland surface
 1078 mass balance. *The Cryosphere Discuss..* doi: 10.5194/tc-2018-257
- 1079 Wan, H., Giorgetta, M. A., Zängl, G., Restelli, M., Majewski, D., Bonaventura, L.,
 1080 ... others (2013). "the icon-1.2 hydrostatic atmospheric dynamical core on
 1081 triangular grids, part i: formulation and performance of the baseline version".
 1082 *Geosci. Model Dev.*, 6, 735–763.
- 1083 Williamson, D. (2007). The evolution of dynamical cores for global atmospheric
 1084 models. *J. Meteor. Soc. Japan*, 85, 241–269.
- 1085 Williamson, D. (2008). Convergence of aqua-planet simulations with increasing res-
 1086 olution in the community atmospheric model, version 3. *Tellus A*, 60(5), 848–
 1087 862. doi: 10.1111/j.1600-0870.2008.00339.x
- 1088 Zarzycki, C. M., Jablonowski, C., & Taylor, M. A. (2014). Using variable-resolution
 1089 meshes to model tropical cyclones in the community atmosphere model. *Mon.
 1090 Wea. Rev.*, 142(3), 1221–1239. doi: 10.1175/MWR-D-13-00179.1
- 1091 Zhang, G., & McFarlane, N. (1995). Sensitivity of climate simulations to the
 1092 parameterization of cumulus convection in the canadian climate center general-
 1093 circulation model. *ATMOSPHERE-OCEAN*, 33(3), 407–446.

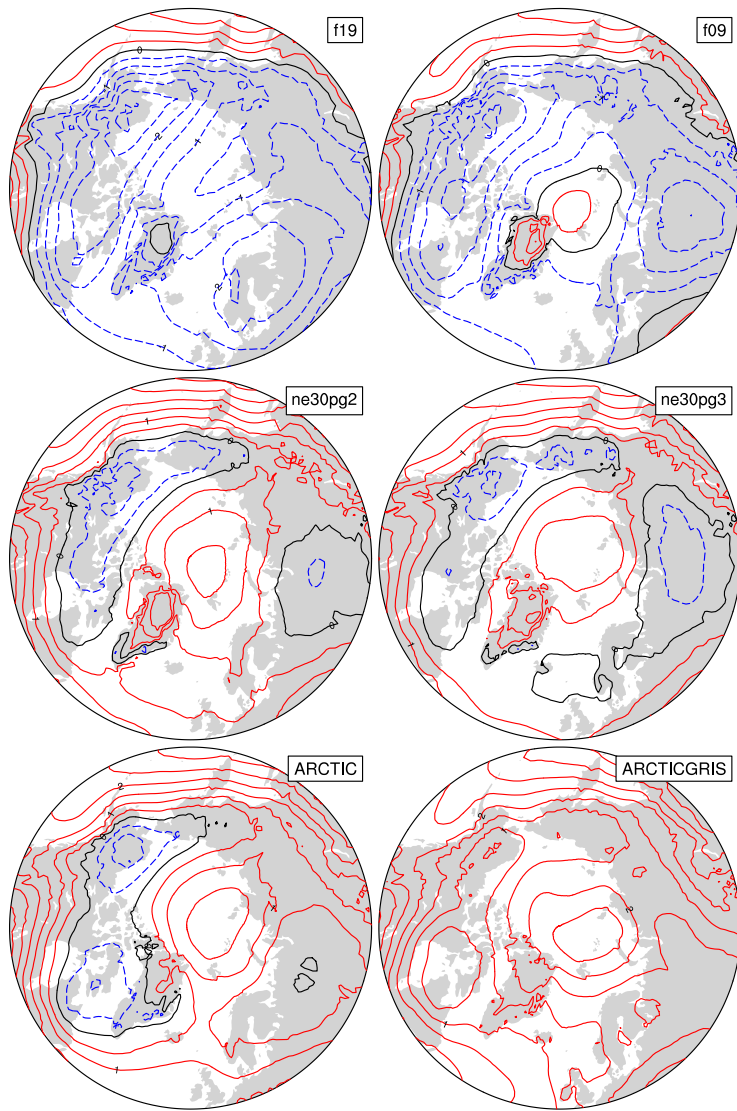


Figure 6. 1979-1998 lower troposphere, northern hemisphere summer virtual temperature biases, computed as the difference from ERA5. Lower troposphere layer mean virtual temperature is derived from the 1000 hPa - 500h Pa geopotential thickness, using the hypsometric equation. Differences are computed after mapping the ERA5 data to the finite-volume grids since the geopotential field is only available on the output tapes in the spectral-element runs that have been interpolated to the f09 grid, inline.

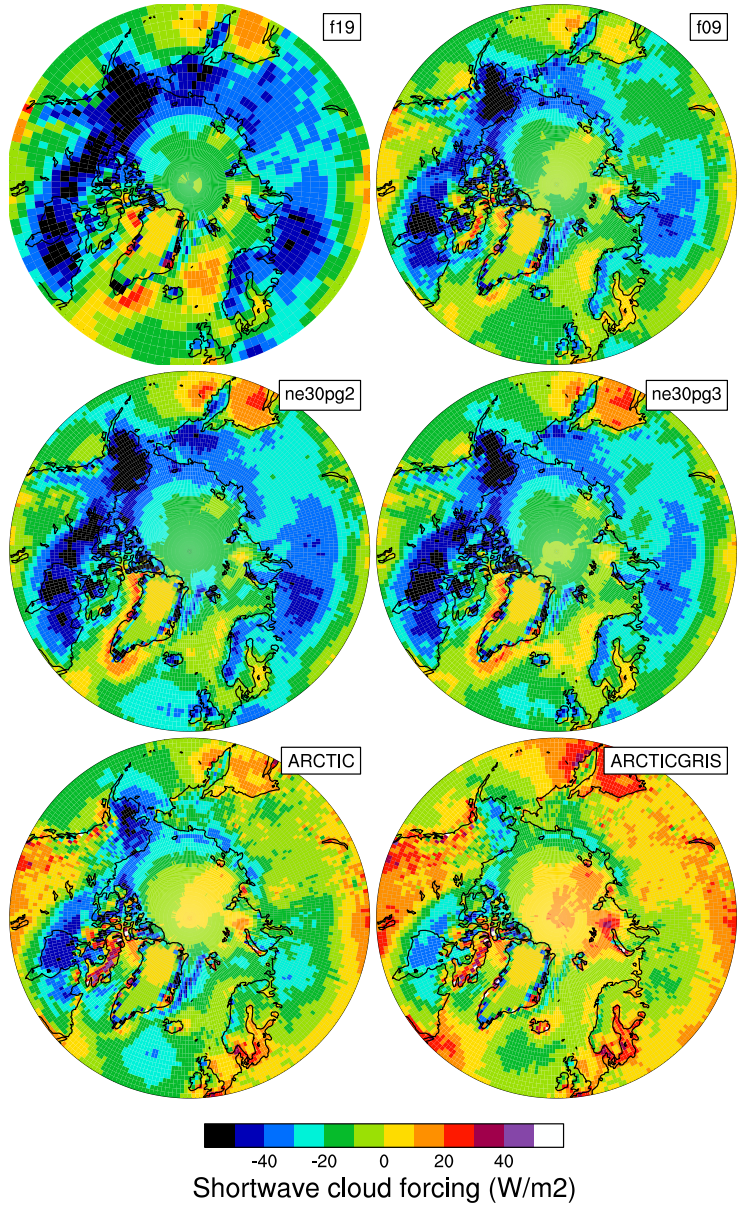


Figure 7. 1979-1998 Northern Hemisphere summer shortwave cloud forcing bias, relative to the CERES-EBAF gridded dataset. Shortwave cloud forcing is defined as the difference between all-sky and clear-sky net shortwave fluxes at the top of the atmosphere. Differences are computed after mapping all model output to the 1° CERES-EBAF grid.

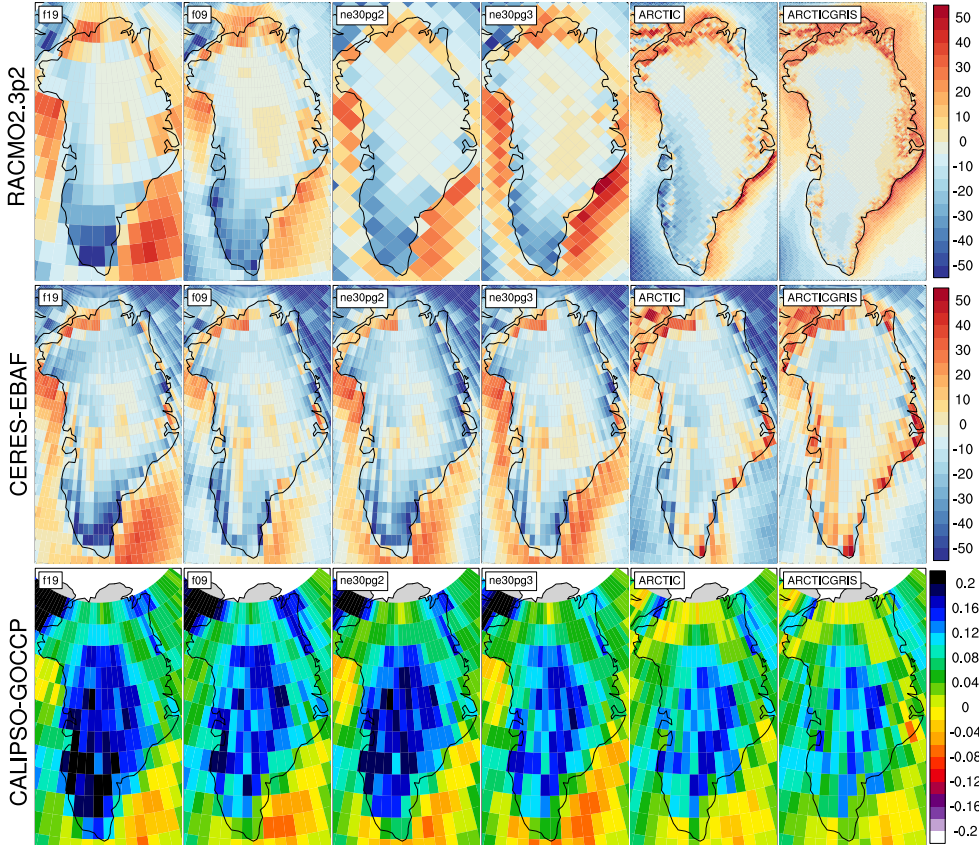


Figure 8. 1979-1998 northern hemisphere summer surface incident shortwave radiation bias (W/m^2), computed as the difference (top) from CERES, and (middle) RACMO2.3p2 dataset, and the (bottom) total cloud fraction bias relative to the CALIPSO dataset. CALIPSO and CERES differences are found by mapping the model output to the 1° grid, and differences in the bottom panel are computed after mapping the RACMO2.3p2 dataset to the individual model grids. Note that the averaging period for the CALIPSO-GOCCP and CERES-EBAF panels, 2006-2017 and 2003-2020, respectively, are different from the averaging period for the model results.

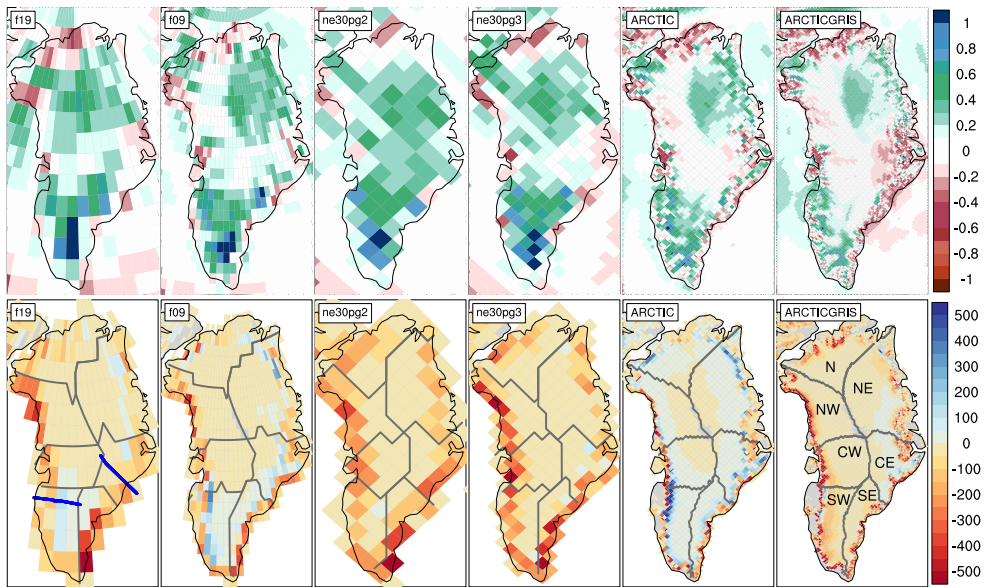


Figure 9. 1979-1998 (top) annual precipitation and (bottom) ice/snow melt biases relative to RACMO2.3p2, evaluated on the native model grids. The precipitation biases are expressed as fractional changes, whereas the melt biases are absolute changes (mm/yr). In the bottom panel, the Rignot and Mouginot (2012) basin boundaries are shown in grey for each model grid. Note that Figure 11 uses the basin boundaries for the two common ice masks, shown in the f19 and ne30pg2 panels, in computing the basin-scale integrals. Blue lines in the f19 panel show the location of the two transects plotted in Figure 12..

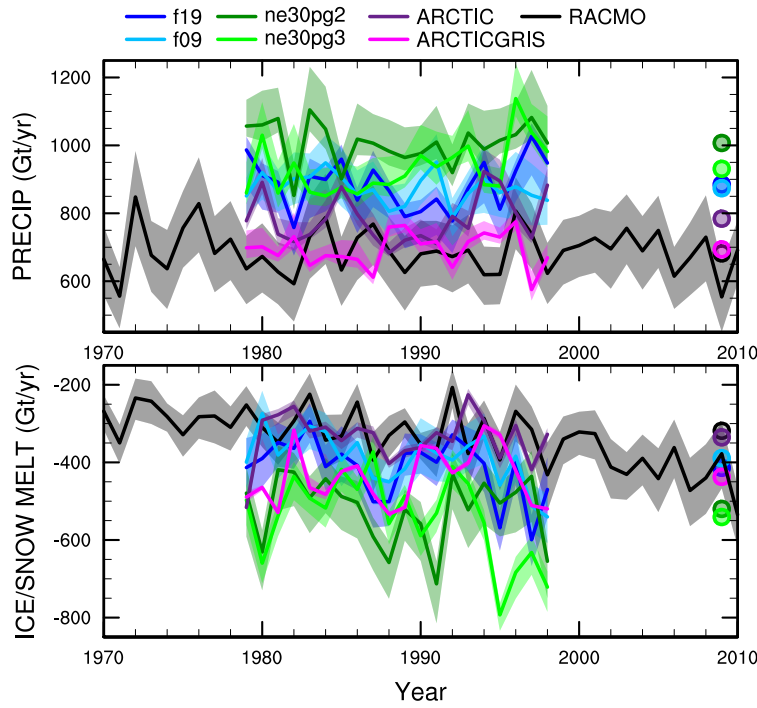


Figure 10. Time-series of annual (solid+liquid) precipitation (top) and annual runoff (bottom) integrated over the Greenland Ice Sheet for all six simulations and compared to the RACMO datasets. The time-series were generated using the common ice mask approach, which results in up to 4 ensembles, with the mean value given by the solid line and shading spanning the extent of the ensemble members.

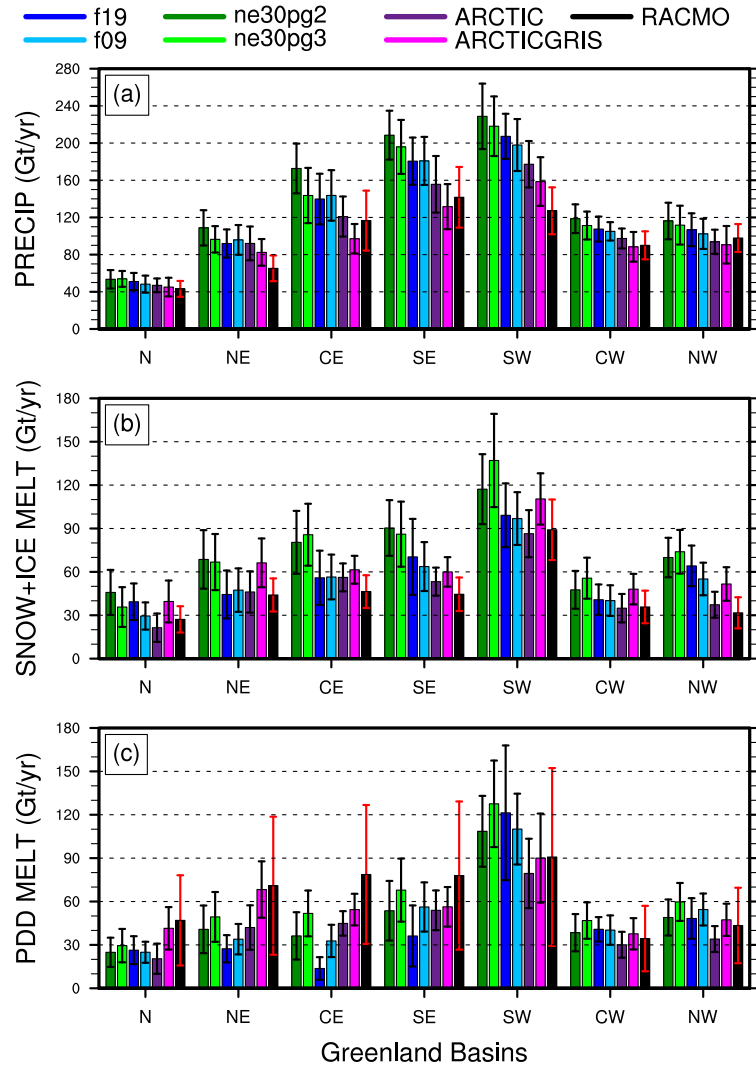


Figure 11. 1979–1998 basin integrated components of the SMB; (top) precipitation, (middle) ice/snow melt and (bottom) ice/snow melt estimated from the PDD method. Whiskers span the max/min of the four ensemble members generated from the common-ice-mask approach. Basin definitions are after Rignot and Mouginot (2012), and are found on the common ice masks using a nearest neighbor approach, and shown in Figure 9.

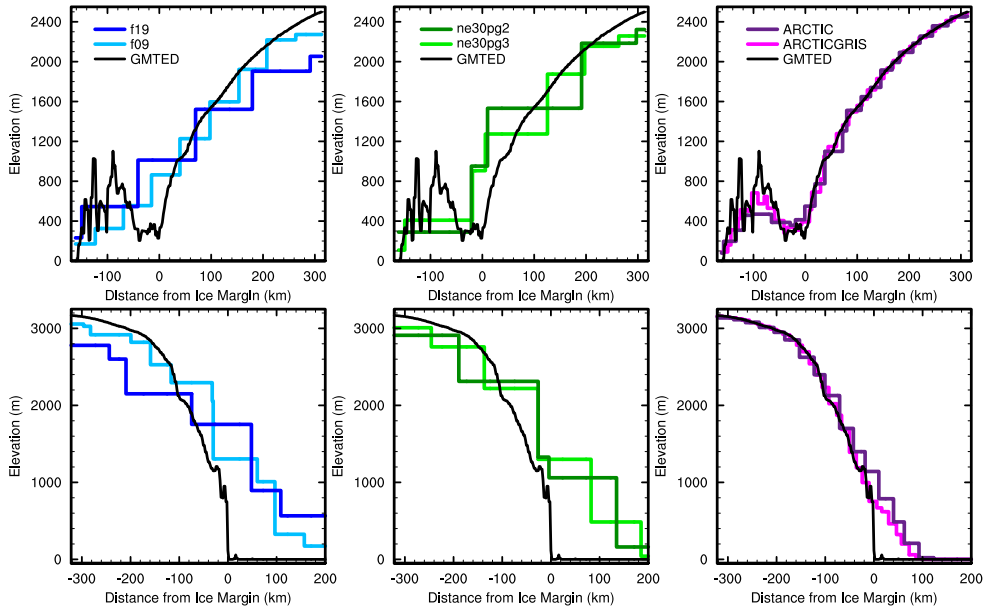


Figure 12. Model surface elevation along the (top) K-transect, and (bottom) a transect spanning the central dome down to the Kangerlussuaq glacier in southeast Greenland, for all model grids. The GMTED reference surface is a 1 km surface elevation dataset (J. Danielson & Gesch, 2011) used for generating the CAM topographic boundary conditions.

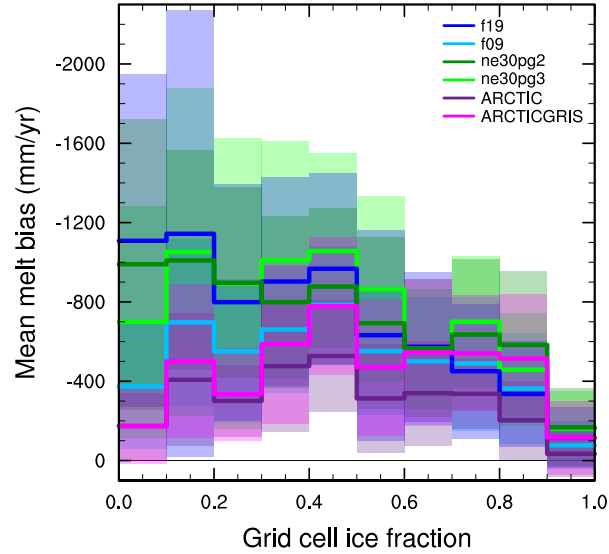


Figure 13. Fractional melt bias over the GrIS, computed relative to the RACMO datasets using the common ice mask approach, and conditionally sampled by grid cell ice fraction provided by the common ice masks. Solid lines are the mean of the distribution with \pm one standard deviation expressed by shading.

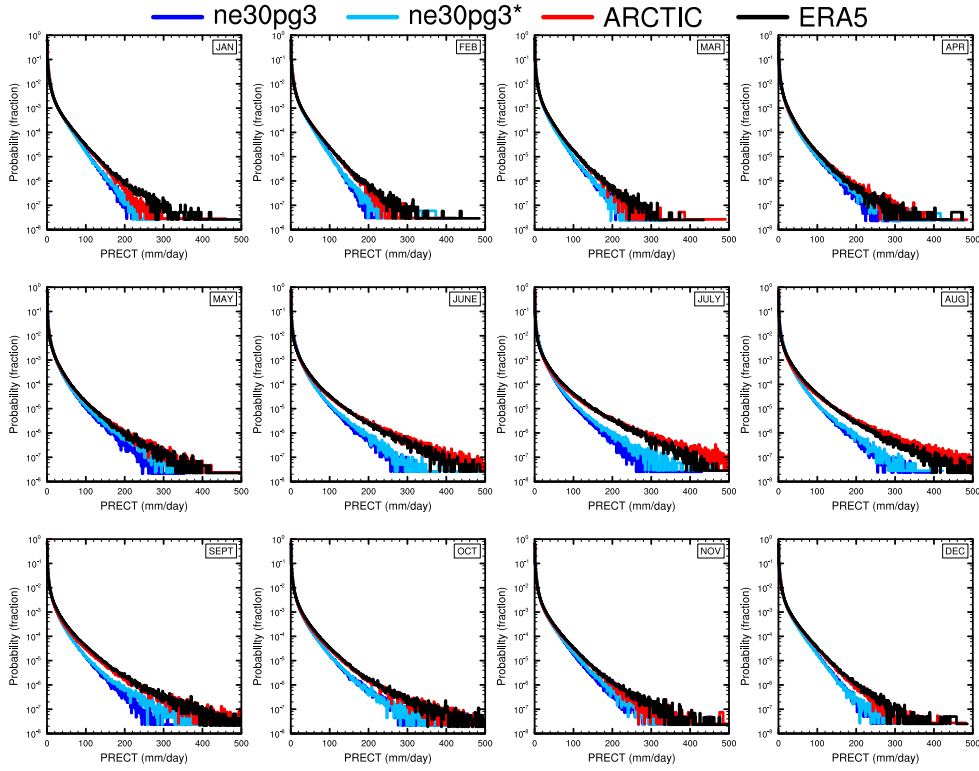


Figure 14. PDFs of the total precipitation rate associated with tracked storms, by month, in the ne30pg3, ne30pg3* and Arctic runs, and compared with the ERA5 dataset.

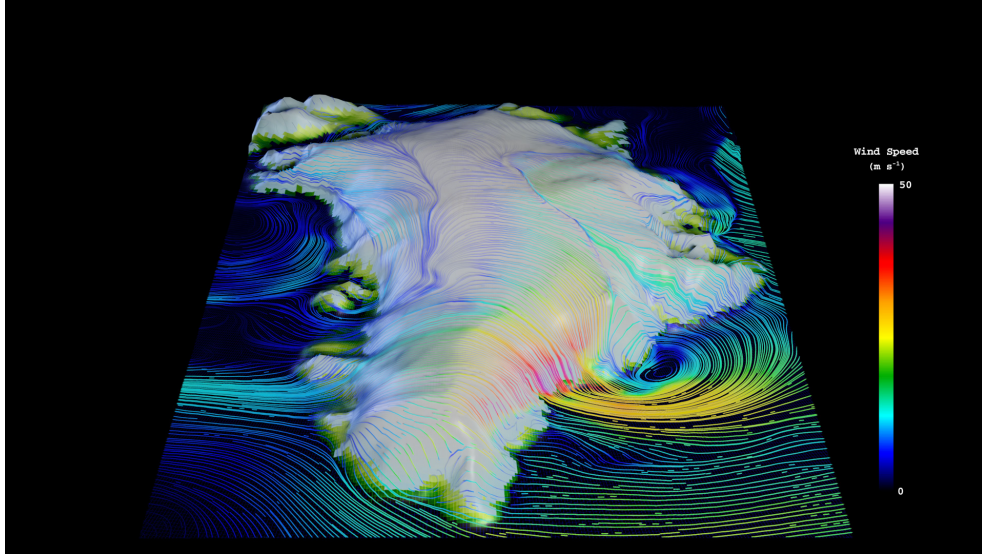


Figure 15. Snapshot of the lowest model level streamlines from the Arctic – GrIS visualization, with color shading denoting the wind magnitude.

OMEGA500, 1 year average, F2000climo, 32 levels

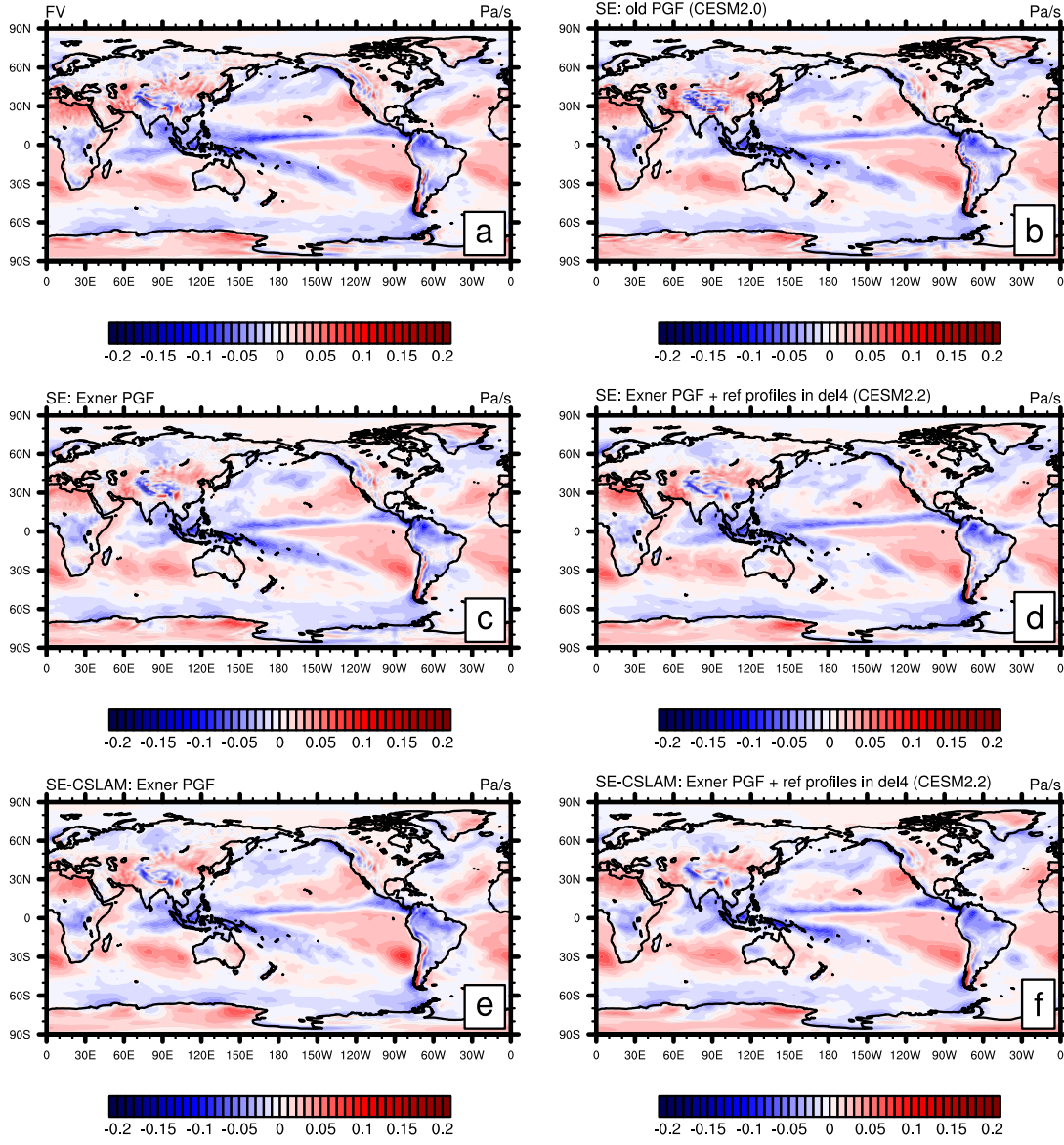


Figure A1. One year averages of vertical pressure velocity at 500hPa (OMEGA500) using (a) CAM-FV (Finite-Volume dynamical core) and (b-f) various versions of the spectral-element (SE) dynamical core at approximately 1° horizontal resolution and using 32 levels. (b) is equivalent to the CESM2.0 version of the SE dynamical core using the "traditional"/"old" discretization of the pressure-gradient force (PGF). Plot (c) is equivalent to configuration (b) but using the Exner form of the PGF. Plot (d) is the same as configuration (c) but also subtracting reference profiles from pressure and temperature before applying hyperviscosity operators (which is equivalent to the CESM2.2 version of SE in terms of the dynamical core). Plots (e) and (f) are equivalent to (c) and (d), respectively, by using the SE-CSLAM (ne30pg3) version of the SE dynamical core (i.e. separate quasi-uniform physics grid and CSLAM transport scheme).

OMEGA500, 18 months average, FHS94 forcing, 32 levels

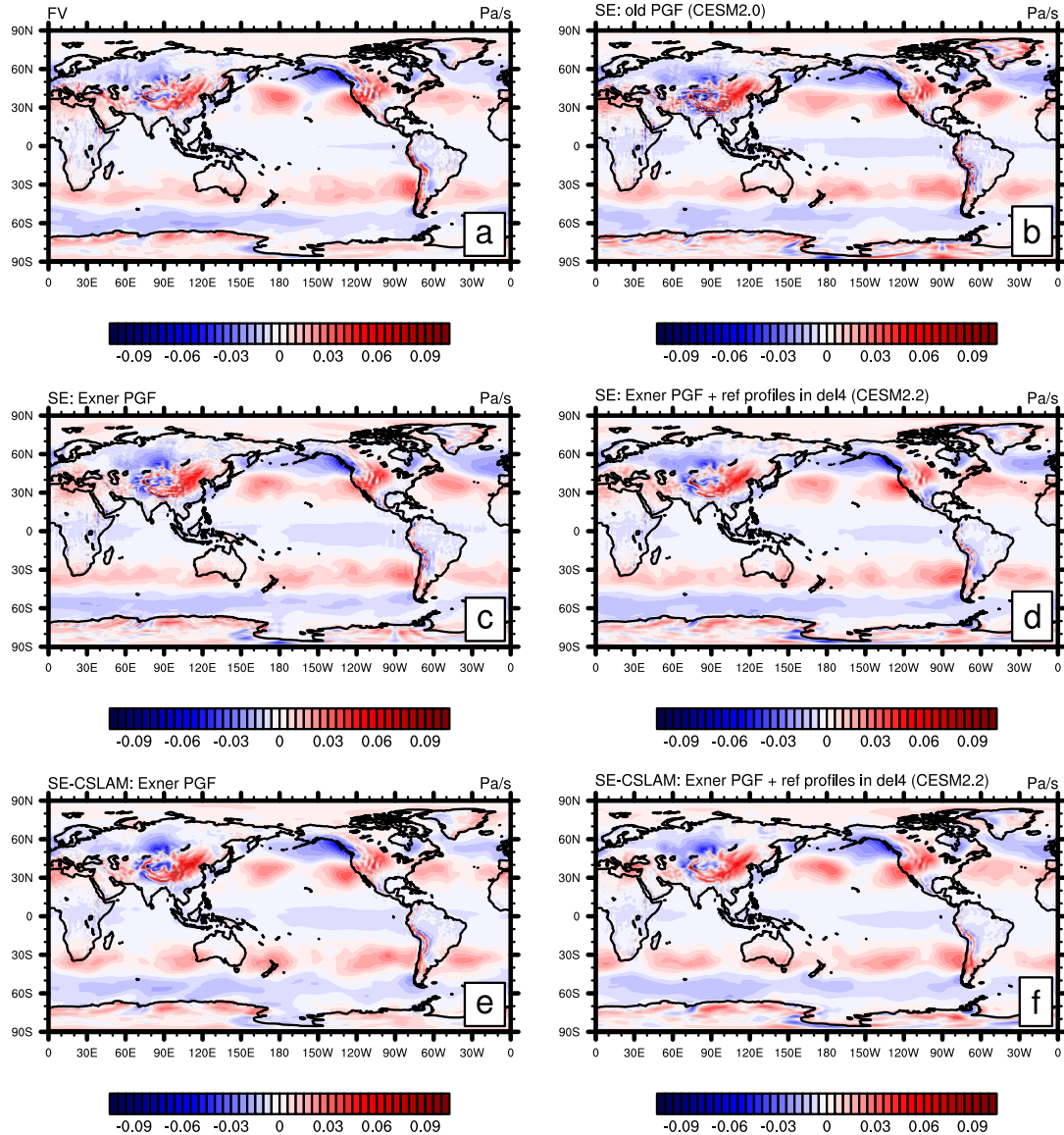


Figure A2. Same as Figure A1 but using modified Held-Suarez forcing and the average is over 18 months (excl. spin-up).